Slow earthquakes: Tectonic tremor, low-frequency earthquakes and slow slip events

Ariane Ducellier
PhD Dissertation Proposal
October 25th 2019

1 Introduction

The largest earthquakes on Earth occur in subduction zones, where large segments of the boundary between the subducting tectonic plate and the overlying plate can store energy for centuries and then release it in minutes during an earthquake. To better assess the seismic hazard, it is thus necessary to improve our understanding of subduction zone processes. Slow earthquakes are a new feature discovered in the last two decades in many subduction zones thanks to the deployment of continuously recording global positioning system (GPS) networks, and high-sensitivity borehole seismometer arrays. They can last from a few days to several years, and have a relatively short recurrence time (months to years), compared to the recurrence time of regular earthquakes (up to several hundreds of years), allowing scientists to observe and study many complete event cycles, which is typically not possible to explore with traditional earthquake catalogs.

Moreover, whereas megathrust earthquakes occur on the locked section of the subduction zone, slow earthquakes often occur downdip on the plate boundary. Interactions between the slow earthquakes zone and the seismogenic zone could potentially trigger large earthquakes. This phenomenon complicates our understanding of subduction zone processes, and should be taken into account when studying the seismic hazard.

As ordinary earthquakes, slow slip events are caused by slip on a fault such as the plate boundary between a tectonic plate subducting under another tectonic plate. However, they take a much longer time (several days to several years) to happen relative to ordinary earthquakes, and the seismic waves they generate are much weaker than the seismic waves generated by ordinary earthquakes, and may not be detectable. A slow slip event on the plate boundary is inferred to happen when there is a reversal of the direction of motion at GPS stations, compared to the secular motion of the surface displacement. Slow slip events have been observed in many subduction zones, such as Cascadia, Nankai (southwest Japan), Alaska, Costa Rica, Mexico, and New Zealand (Beroza and Ide, 2011 [8]; Audet and Kim, 2016 [5]).

In many places, tectonic tremor are also observed in relation to slow slip. Tremor is a long (several seconds to many minutes), low amplitude seismic signal, with emergent onsets, and an absence of clear impulsive phases. Tectonic tremor have been explained as a swarm of small, low-frequency earthquakes (LFEs ; Shelly *et al.*, 2007 [61]), that is small magnitude earthquakes (M $\sim$ 1) which frequency content (1-10 Hz) is lower than for ordinary earthquakes (up to 20 Hz). The source of the LFEs is located on the plate boundary, and their focal mechanisms represent shear slip on a low-angle thrust fault dipping in the same direction as the plate interface (Ide *et al.* [33]). Due to the lack of clear impulsive phases in the tremor signal, it is difficult to determine the depth of the tremor source with the same precision, and it is assumed to be also located close to the plate

boundary.

LFEs are usually grouped into families of events, with all the earthquakes of a given family originating from the same small patch on the plate interface, and recurring more or less episodically in a bursty manner. The recurrence behavior of LFE families varies a lot between seismic regions, and inside the same seismic region. In Washington State, LFE swarm duration, recurrence interval, and number of LFEs per swarm decrease systematically with increasing depth (Sweet *et al.*, 2019 [64]). On the San Andreas Fault, the recurrence behaviors of LFE families vary from highly episodic (large episodes every few months) to semicontinuous (small episodes every few days), and some LFE families exhibit variability in recurrence behavior over time, from semicontinuous to episodic (Shelly, 2017 [60]).

In subduction zones such as Nankai and Cascadia, tectonic tremor observations are spatially and temporally correlated with slow slip observations (Obara, 2002 [46]; Rogers and Dragert, 2003 [53]). Due to this correlation, these paired phenomena have been called Episodic Tremor and Slip (ETS). However, in Cascadia only the biggest tremor episodes are associated with slow slip events. Smaller slow slip events may occur at the same time as the smaller bursts of tremor, but if they exist, they are currently undetected. Moreover, in northern New Zealand, tremor and slow slip do not seem to be spatially and temporally correlated. Tremor is more challenging to detect, seems to be located downdip of the slow slip on the plate boundary, and the tremor activity does not seem to increase during slow slip events.

2 Proposed PhD Research

The purpose of my research is to carry out data analyses of recordings of tectonic tremor, low-frequency earthquakes and slow slip events to better understand the mechanism of slow earthquakes. Specifically, I intend to answer the following questions:

- Is the source of the tectonic tremor located on the plate boundary? What is the depth extent of the location of the source of the tremor?
- Do low-frequency earthquakes families behave similarly or differently in Northern California, compared to Washington State and the San Andreas Fault?
- Can we detect smaller and / or longer slow slip events using geodetic data in the absence of spatially and temporally correlated tectonic tremor?

My PhD thesis will be comprised of five chapters. The first chapter will be an introduction and literature review of slow earthquake phenomena. The second, third, and fourth chapters will be journal articles detailing the methods used to answer the previous questions, and what it can tell us on the causes and mechanisms of slow earthquakes. The final chapter will synthesize my research into conclusions and potential future avenues of research.

2.1 Depth of the source of the tectonic tremor in the northeastern Olympic Peninsula

Is the source of the tectonic tremor located on the plate boundary? What is the depth extent of the location of the source of the tremor?

2.1.1 Introduction

Tremor is a long (several seconds to many minutes), low amplitude seismic signal, with emergent onsets, and an absence of clear impulsive phases. Tectonic tremor have been explained as a swarm of small, low frequency earthquakes (LFEs) [61], that is small magnitude earthquakes ($M \sim 1$) which frequency content (1-10 Hz) is lower than for ordinary earthquakes (up to 20 Hz). The source of LFEs is located on the plate boundary, and their focal mechanisms represent shear slip on a low-angle thrust fault dipping in the same direction as the plate interface [33]. Due to the lack of clear impulsive phases in the tremor signal, it is difficult to determine the depth of the tremor source with the same precision, and it is assumed to be also located close to the plate boundary. In subduction zones such as Nankai and Cascadia, tectonic tremor observations are spatially and temporally correlated with slow slip observations [46, 53]. Due to this correlation, these paired phenomena have been called Episodic Tremor and Slip (ETS).

The occurrence of tremor seems to be linked to low effective normal stress or high fluid pressure near the location of the source of the tremor. Indeed, Shelly *et al.* (2006 [62]) have observed a high ratio between P-wave velocity and S-wave velocity in the subducting oceanic crust near the location of the LFEs in western Shikoku, Japan. They hypothesized that the source of the fluids is the dehydration of hydrous minerals within the subducting oceanic crust. In Cascadia, Audet *et al.* (2009 [3]) have computed receiver functions of teleseismic waves in Vancouver Island, and analyzed the delay times between the forward-scattered P-to-S, and back-scattered P-to-S and S-to-S conversions at two seismic reflectors identified as the top and bottom of the oceanic crust. It allowed them to compute the P-to-S velocity ratio of the layer and the S-wave velocity contrast at both interfaces. The very low Poisson's ratio of the layer could not be explained by the mineral composition, and they interpreted it as evidence for high pore-fluid pressure. They explained the sharp velocity contrast on top of the layer as a low permeability boundary between the oceanic plate and the overriding continental crust. They hypothesized that the low permeability of the plate interface may be due either to grain-size reduction or to the precipitation of minerals from migrating fluids. At greater depth, the large volume reduction and water release accompanying eclogitization in the subducted oceanic crust, and the large volume expansion accompanying serpentinization in the mantle wedge, could increase the permeability of the plate boundary through fracture generation. A possible cause of ETS events could be periodic cycles of steady pore-fluid pressure build-up from dehydration of subducted oceanic crust, fluid release from fracturing of the interface during ETS, and subsequent precipitation sealing of the plate boundary.

Moreover, the variations of tremor occurrence have been linked to tidal cycles. Nakata *et al.* (2008 [44]) noticed that tremor swarms often exhibit occurrences with a periodicity of about 12 or 24 h, and concluded that they are probably related to Earth tides. Their occurrence is also well correlated with time evolution of Coulomb failure stress (CFS) and CFS rate. However, they noted

that tremor occurrences are advanced by a few hours relative to CFS, from which they conclude that a simple Coulomb threshold model is not sufficient to explain tremor occurrence. Instead they point out that the correlation of tremor occurrence and the CFS rate as well as the time delay between both could be reproduced by using the rate- and state-dependent friction law. Thomas *et al.* (2009 [70]) have also observed that tremor occurrence on the deep San Andreas fault are correlated with small, tidal shear stress changes. They explain it by a very weak fault zone with low effective normal stress, probably due to near-lithostatic pore pressures at the depth of the tremor source region.

Shelly *et al.* (2006 [62]) made two hypothesis explaining how highly pressured fluids could generate tectonic tremor. A first possibility is that tremor is generated by the movement of fluids at depth, either by hydraulic fracturing or by coupling between the rock and fluid flow. The accompanying slip could be triggered by the same fluid movement that generates the tremor or, alternatively, the fluid flow could be a response to changes in stress and strain induced by the accompanying slip. The second possibility is that tremor is generated by slow otherwise aseismic shear slip on the plate interface as slip locally accelerates owing to the effects of geometric or physical irregularities on the plate interface. Fluids would then play an auxiliary role, altering the conditions on the plate interface to enable transient slip events, without generating seismic waves directly.

Fagereng and Diener (2011 [17]) have explained why the generation of tectonic tremor is restricted to a small range of depth along the plate boundary by computing the equilibrium mineral assemblages at different P-T conditions, and comparing it to the P-T path of the subducting oceanic crust in Shikoku and Cascadia. They noted that for most of the P-T path, there are no dehydration reactions and the slab remains fluid-absent, except for depths between 30 and 35 km depth for Shikoku, and depths between 30 and 40 km for Cascadia, where the mineral model predicts significant water release. These depth ranges coincide with the depth range where tremor has been observed. They concluded that abundant tremor activity requires metamorphic conditions where localized dehydration occurs during subduction, and that subduction zones where dehydration reactions are more widely distributed will produce a more diffuse pattern of tremor activity that would be harder to detect.

Moreover, the generation of slow slip and tectonic tremor has been related to the presence of quartz in the overriding continental crust. Indeed, Audet and Bürgemann (2014 [4]) studied the relationship between the ratio between P-wave velocity and S-wave velocity in the subducted oceanic crust and the forearc and the periodicity of slow earthquakes. They computed the V_P/V_S ratio from receiver functions and data from the literature. They noticed that slow earthquakes are associated with a high V_P/V_S ratio in the subducted oceanic crust, but without relationship with recurrence time. However, they pointed out that the recurrence time of slow earthquakes increases linearly with the V_P/V_S ratio of the forearc. Moreover, along a margin-perpendicular profile from northern Cascadia, the V_P/V_S ratio of the forearc, and the recurrence time of Episodic Tremor and Slip (ETS) events, decrease with increasing depth. The authors explained the low V_P/V_S ratio in the forearc by the enrichment of forearc minerals in fluid-dissolved silica derived from the dehydration of the downgoing slab. However, they estimated that the fluid flux required for the formation of quartz veins was two orders of magnitude greater than the fluid production rates estimated from

the dehydration of the slab. They hypothesized that silica-saturated fluids may originate from the complete serpentinization of the mantle near the wedge corner. They suggested that higher temperature and quartz content at depth may lead to faster dissolution - precipitation processes and more frequent slip events. Their model could also explain the global variation in recurrence time, with mafic silica-poor regions having longer ETS recurrence times that felsic silica-rich regions.

Hyndman *et al.* (2015 [31]) have also investigated the processes that control the ETS in the Cascadia subduction zone. They noticed that the high temperatures in the young subducting oceanic plate, the geodetic data, and the recordings of coseismic subsidence in buried coastal marshes during past great earthquakes, all point out to a downdip limit of the seismogenic zone located offshore. The position of the slow slip and the tremor is well known, although the depths have some uncertainty. The slip may extend seaward of the tremor, but there is a clear separation between the seismogenic zone and the ETS zone, with the ETS zone being located about 70 km east of the downdip limit of the seismogenic zone, and the volcanic arc being located about 100 km east of the ETS zone. A previous study showed that the position of the subduction zone ETS does not coincide with a specific temperature or dehydration reaction. The authors pointed out that ETS has been related to high pore fluid pressures close to the plate boundary. They argued that the bending of the subducting plate at the ocean trench may introduce a large amount of water in the upper oceanic mantle, resulting in extensive serpentinization. Moreover, the serpentinization of the fore-arc mantle corner may increase its vertical impermeability, while keeping a high permeability parallel to the fault, thus channelling all the fluid updip in the subducting oceanic crust. The dehydration of the serpentinite from the upper oceanic mantle, and the focusing of rising fluids along the plate boundary should result in large amounts of fluids available at the fore-arc mantle corner. Additionally, there seems to be a good coincidence between the location of the fore-arc mantle corner, and the location of ETS. The authors then observed that the deep fore-arc crust has a very low Poisson's ratio (less than 0.22), and that the only mineral with a very low Poisson's ratio is quartz (about 0.1), which led them to conclude that there may be a significant amount of quartz (about 10 % in volume) in the deep fore-arc crust above the fore-arc mantle. Moreover, as the solubility of silica increases with temperature, fluids generated at depth and rising up the subduction channel should be rich in silica. The authors concluded that there may be a relation between quartz veins formation in the deep fore-arc crust and ETS. However, several constraints as the magnitude and mechanism of the LFEs, and the vertical extent of the tremor should be explained.

Quartz veins have indeed been observed in exhumed subduction zone. For instance, Fagereng *et al.* (2014 [18]) have studied an exhumed shear zone representing the subduction megathrust before its incorporation into the accretionary prism. They focused their study on a 30 m high by 80 m long cliff exposure where foliation has developed as a result of shearing along the subduction thrust interface. They identified two groups of quartz veins, foliation-parallel veins, and discordant veins, that must have formed for an extended time before, during, and after foliation development. They interpret the foliation-parallel veins as having been formed by viscous shear flow, and note that the shear stain rate due to the flow may be high enough to accommodate a slow slip strain rate of $\sim 10^{-9}s{-}1$, for a typical subduction thrust thickness of 30 m (Rowe *et al.*, 2013 [55]). They interpret the discordant veins as having been formed by brittle deformation caused by locally elevated fluid pressure. The size of the structures where brittle deformation is observed (meters to hundreds of meters) is compatible with the size of the asperity rupturing during an LFE. Tremor

and slow slip may thus be a manifestation of brittle-viscous deformation in the shear zone.

However, the zone with high low Poisson's ratio observed by Hyndman *et al.* (2015 [31]) has a large vertical extent (about 10 kilometers). If the whole zone is associated with quartz deposition and tectonic tremor generation, we should also observe a large vertical distribution of the source of the tremor. Kao *et al.* (2006 [36]) have used a Source Source Scanning Algorithm to detect and locate tremor, and have indeed located tremor in the continental crust, with a wide depth range of over 40 km. They noted that this wide depth range could not arise from either analysis uncertainties or a systematic bias in the velocity model they used. A follow-up study by Kao *et al.* (2009 [35]) gave a thickness of the tremor zone of 5-10 km. This depth range is inconsistent with the depth of the LFEs, which have been located on a thin band at or near the plate interface with a rupture mechanism that corresponds to the thrust dip angle (Ide *et al.*, 2007 [33]). Further study is thus needed to narrow the uncertainty on the depth of the source of the tremor, and verify whether tremor could occur in a wider zone than LFEs.

Several methods have been developed to detect and locate tectonic tremor or LFEs using the cross correlation of seismic signals. The main idea is to find similar waveforms in two different seismic signals, which could correspond to a single tremor or LFE recorded at two different stations, or two different tremors or LFEs with the same source location but occurring at two different times and recorded by the same station. A first method consists in comparing the envelopes of seismograms at different stations (Obara, 2002 [46]; Wech and Creager, 2008 [77]), or directly the seismograms at different stations (Rubin and Armbruster, 2013 [57]). For instance, Wech and Creager (2008 [77]) computed the cross correlations of envelope seismograms for a set of 20 stations in western Washington and southern Vancouver Island. Then, they performed a grid search over all possible source locations to determine which one minimizes the difference between the maximum cross correlation and the value of the correlogram at the lag time corresponding to the S-wave travel time difference between two stations.

A second method is based on the assumption that repeating tremor or LFEs with sources located nearby in space will have similar waveforms (Bostock *et al.*, 2012 [9]; Royer and Rostock, 2014 [56]; Shelly *et al.*, 2006 [62]; Shelly *et al.*, 2007 [61]). For instance, Bostock *et al.* (2012 [9]) looked for LFEs by computing autocorrelations of 6-second long windows for each component of 7 stations in Vancouver Island. They then classified their LFE detections into 140 families. By stacking all waveforms of a given family, they obtained an LFE template for each family. They extended their templates by adding more stations and computing cross correlations between station data and template waveforms. They used P- and S-traveltime picks to obtain an hypocenter for each LFE template. By observing the polarizations of the P- and S-waveforms of the LFE templates, they computed focal mechanisms and obtained a mixture of strike slip and thrust mechanisms, corresponding to a compressive stress field consistent with thrust faulting parallel to the plate interface. Further study showed that the average double couple solution is generally consistent with shallow thrusting in the direction of plate motion [56].

Finally, a third method uses seismograms recorded across small-aperture arrays (Ghosh *et al.*, 2010 [25]; La Rocca *et al.*, 2009 [38]). For instance, La Rocca *et al.* (2009 [38]) stacked seismograms over all stations of the array for each component, and for three arrays in Cascadia.

They then computed the cross-correlation between the horizontal and the vertical component, and found a distinct and persistent peak at a positive lag time, corresponding to the time between P-wave arrival on the vertical channel and S-wave arrival on the horizontal channels. Using a standard layered Earth model, and horizontal slowness estimated from array analysis, they computed the depths of the tremor sources. They located the sources near or at the plate interface, with a much better depth resolution than previous methods based on seismic signal envelopes, source scanning algorithm, or small-aperture arrays. They concluded that at least some of the tremor consisted in the repetition of LFEs as was the case in Shikoku. A drawback of the method was that it could be applied only to tremor located beneath an array, and coming from only one place for an extended period of time.

2.1.2 Data

The data were collected during the 2009-2010 Array of Arrays experiment. Eight small-aperture arrays were installed in the northeastern part of the Olympic Peninsula, Washington. The aperture of the arrays was about 1 km, and station spacing was a few hundred meters. The arrays were around 5 to 10 km apart from each other (Figure 1). Most of the arrays were installed for more than a year, between June 2009 to September 2010, and were able to record the main August 2010 ETS event. Some of the arrays were also recording during the August 2011 ETS event. Ghosh *et al.* (2012 [23]) used a multibeam-backprojection (MBBP) technique to detect and locate tremor. They bandpass filtered the vertical component between 5 and 9 Hz. They divided the data into one-minute-long sliding independent (no overlap) time windows. They performed beam forming in the frequency domain at each array to determine the slowness vectors, and backprojected the slownesses in the 3-D space to locate the source of the tremor for each time window. We thus have two catalogs of tremors. The first one is a catalog of 28902 one-minute-long time windows during which tremor was detected between June 20th 2009 and September 30th 2010. For each time window, we have the beginning time, the end time, and the location (latitude and longitude) of the source of the tremor. The second one is a catalog of 5600 one-minute-long time windows between August 10th 2011 and September 6th 2011.

2.1.3 Method

We took a 5 km by 5 km grid cell located not too far (less than 25 km) from a given array. We then took all the one-minute-long time windows when tremor was detected and the source of the tremor was located inside this cell. For each one-minute-long time window, we downloaded the seismic data for each seismic station of the array. Then, for each seismic station and each channel, we detrended the data, tapered the first and last 5 seconds of the data with a Hann window, removed the instrument response, bandpass filtered between 2 and 8 Hz, and resampled the data to 20 Hz. All these preprocessing operations were done with the Python package obspy. For each seismic station and each one-minute-long time window, we cross correlated the vertical component with the East-West horizontal component and the North-South horizontal component. Then, we stacked the cross correlation functions over all the seismic stations of the array. We experimented with a linear stack, a n-root stack, and a phase-weighted stack. Figure 2 shows an example of the cross correlation functions as a function of time for the Big Skidder array for the 82 one-minute long time windows when tremor was detected in a 5 km by 5 km grid cell centered on the array. We can

see that for about half of the tremor windows, there is a peak in the cross correlation at about 4.7 s. As the energy of the P-waves is expected to be higher on the vertical component, and the energy of the S-waves to be higher on the horizontal components, we assume that this peak corresponds to the time lag between the arrival a direct P-wave and a direct S-wave. We then stacked the cross correlation functions over all the one-minute-long time windows. Again, we experimented with a linear stack, a power stack, and a phase-weighted stack. We assume that the time of the maximum absolute value of the peak of the stack is the time lag between the arrival of the direct P-wave and the arrival of the direct S-wave.

Only about half of the cross correlation functions have a distinct peak that coincides with the peak in the stacked cross correlation. The other cross correlations functions show either a distinct peak at another time lag, or no clearly visible peak. This may be either because the source of the tremor during the corresponding one-minute-long time window was mislocated, or because the signal-to-noise ratio is too low. To improve the signal-to-noise ratio of the peak in the stacked cross correlation, we divided the one-minute-long time windows into two clusters, the ones that match well the stacked cross correlation, and the ones that do not match it well. For each one-minute-long time window, we computed the maximum absolute value of the cross correlation, its value at time 0, the time at which it takes its maximum absolute value, and the ratio between the amplitude of the cross correlation peak to the root mean square of the cross correlation function. We did this for both the East-West component and the North-South component. Each one-minute-long time window is thus associated to eight values of quality criteria. We then classified each one-minute-long time window into two different clusters, based on the value of these criteria, using a K-means clustering algorithm (function sklearn.cluster.KMeans from the Python library SciKitLearn). The K-means procedure is as follows: We choose the number of clusters R, then we arbitrarily choose a center for each cluster. We put each one-minute-long time window into the cluster to which it is closest (based on the values of the eight criteria). Once all one-minute-long time windows have been put in a cluster, we recompute the mean of the eight criteria for each cluster, and reiterate the procedure until convergence. For each cluster, we then stacked the cross correlation functions over all the one-minute-long time windows belonging to the cluster. Figure 3 shows the envelope of the stacked cross correlation for each of the clusters compared to the original stacked cross correlation for all the one-minute-long time windows. The clustering has improved the amplitude of the peak for one of the clusters, and made the peak nearly disappear for the other cluster.

We did this analysis for grid cells located in a 50 km by 50 km area centered on each of the eight arrays. We thus have 11 * 11 * 8 = 968 values of the time lag between the arrival of the direct P-wave and the arrival of the direct S-wave. We first assumed that the source of the tremor is located on the plate boundary, and we took a constant velocity model for the overriding continental crust with V_P = 6.4 km/s and V_S = 3.6 km/s, to compute the depth of the tremor source for each location.

2.1.4 Results

The analysis we carried out above may not lead to a reliable value of the depth of the source of the tremor for all relative positions of the array and the tremor. First, some areas are badly covered, and only a few tremor or no tremor at all were recorded. We limit our analysis to grid cells were

tremor has been recorded during at least 10 one-minute-longtime windows. Second, the method works best for nearly vertical ray paths. A third problem is that we assumed that the location of the tremor source is fixed during the one-minute-long time window where we compute the cross correlation of the seismic signal. However, this is not exactly the case. Indeed, during an ETS event, rapid tremor streaks have been observed propagating in the up-dip and down-dip directions at velocities ranging on average between 30 and 110 km/h (Ghosh *et al.*, 2010 [24]), which corresponds to a maximum source displacement of 0.9 km updip or downdip during the 30 seconds duration before and after the middle of the time window. If we denote t_P the arrival time of the direct P-wave, and t_S the arrival time of the direct S-wave, the time lag between the two phase arrivals is $t_{lag} = t_S - t_P$. During the one-minute time window where we compute the cross correlation, the displacement dx of the tremor source along the plate boundary should corresponds to a time lag difference dt_{lag} shorter than a quarter of the dominant period of the tremor signal T = 0.33 s. We computed the time lag difference for a displacement of the source of 0.9 km in the updip and the downdip directions, for stations aligned along the strike and along the dip direction. We assume that the source was located at 35 km depth, and we look at the time arrivals of the seismic wave for stations located up to 20 km from the epicenter, in the strike or the dip direction. The difference in time lags stays low for all the stations aligned along the strike of the plate boundary. However, for the stations aligned along the dip of the plate boundary, the tremor streaks traveling at 110 km/h will cause a problem for the stations located more than 18 km updip of the tremor source. The difference in time lags stays low for the stations located downdip of the tremor source.

2.1.5 Future work

For each of the grid cells and each of the arrays, I will compute the time lag between the direct P-wave and the direct S-wave by taking the maximum value of the envelope of the stacked cross correlation for the cluster containing the time windows that fit best with the stack. I will compare the value of the time lag for the East-West component and the North-South component, to verify whether possible anisotropy in the overriding continental crust introduce a significant difference between both values of the time lag. I will associate an uncertainty to the time lag by computing the width of the envelope at half the amplitude of the maximum. I will then compute the corresponding depth of the tremor, and the associated uncertainty, for each array using a constant velocity model. I will associate to each grid cell and each array a weight related to the ratio between the maximum amplitude of the stack and the root mean square, and interpolate the values of the depth found for the different arrays while taking these weights into account. I will then be able to obtain a map of the depth of the plate boundary, and compare it to the depth of the LFE families identified by Sweet *et al.* (2019 [64]) and Chestler and Creager (2017a [12] and b [13]).

In the above part, we assumed that all the tremor within a given grid cell originate from the same depth, and we averaged over all the data to get the depth of the tremor source. However, instead of being located on the same plane near the plate boundary, the tremor may be scattered over a layer surrounding the plate boundary. To compute the thickness of this layer, I will compute for each one-minute-long time window for which the cross correlation function matches well the stacked cross correlation the time lag between the time corresponding to the maximum absolute value for the cross correlation function and the time corresponding to the maximum absolute value

for the stacked cross correlation. I will then compute the standard deviation of this time lag, and compute the corresponding difference in depth using the constant velocity model that I used previously. I will thus get the thickness of the layer from which the tremor originate. I will use the same interpolation method as above to get the thickness of the layer for all the area covered by the eight arrays.

2.2 A low-frequency earthquakes catalog for Northern California

Do low-frequency earthquakes families behave similarly or differently in Northern California, compared to Washington State and the San Andreas Fault?

Motivation

The relatively short recurrence of slow slip and tremor events results in a rich history both in space and time and reveals potential patterns. These event histories have allowed scientists to see complete event cycles, which is typically not possible to explore in traditional earthquake catalogs. However, most of the work on low-frequency earthquakes (LFEs) has been focused on detecting LFEs during periods of high tremor activity, grouping them into families of events, and locating the source of the LFE families. Longer catalogs (several years) have been established for LFE families in Mexico (two-year long catalog by Frank *et al.*, 2014 [22]), the San Andreas Fault (fifteen-year-long catalog by Shelly, 2017 [60]), Washington State (five-year-long catalog by Sweet *et al.*, 2019 [64] and two-year-long catalog by Chestler and Creager, 2017a [12] and b [13]), and New Zealand (eight-year-long catalog by Baratin *et al.*, 2018 [7]). These studies have shown that LFEs can show a wide range of different behaviors. In northern Washington, Sweet *et al.* (2019 [64]) have identified and characterized four different LFE families that span the width of the transition zone in the Cascadia Subduction Zone beneath western Washington State. They found that the LFEs swarm duration, recurrence interval, and event size decrease systematically with increasing depth. On the San Andreas Fault, Shelly (2017 [60]) observed a large diversity of recurrence behaviors among the LFE families, from semicontinuous to highly episodic. Particularly, two families exhibited bimodal recurrence patterns (about 3 and 6 days for the first one, and about 2 and 4 days for the second one). Moreover, he observed an increase in the LFE event rate after the 2004 Parkfield earthquake.

Plourde *et al.* (2015 [52]) have detected LFEs in southern Cascadia during the April 2008 Episodic Tremor and Slip (ETS) event using seismic data from the EarthScope Flexible Array Mendocino Experiment (FAME). They used a combination of autodetection methods and visual identification to obtain the initial templates. Then, they recovered higher signal-to-noise LFE signals using iterative network cross correlation. They found that the LFE families on the southern Cascadia Subduction Zone were located above the plate boundary, with a large distribution of depths (28-47 km). Three additional LFE families were found on two strike-slip faults, the Maacama and Bucknell Creek faults, which are part of the San Andreas Fault zone.

I intend to extend the catalog from Plourde *et al.* (2015 [52]) to the whole two years during which the temporary seismic stations from the FAME experiment were installed, (and possibly to

the last 10 years if the quality of the permanent seismic stations allows it) in order to answer two questions:

How are low-frequency earthquake event rates affected by nearby earthquakes? I intend to study how LFE families respond to local perturbations in stress from nearby earthquakes at the Mendocino Triple Junction. The deformation, tectonics, and evolution of southern Cascadia is strongly influenced by the Mendocino Triple Junction, and the Mendocino Triple Junction is one of the most seismically active regions along the Cascadia Subduction Zone. Tremor intensity is affected by regular earthquakes. For instance, tremor in Cascadia is triggered by stresses caused by surface waves from large, distant earthquakes (Rubinstein *et al.*, 2009 [58]), tremor on the San Andreas Fault is triggered by regional earthquakes (Peng *et al.*, 2009 [50]; Guilhem *et al.*, 2010 [27]), and small intraslab earthquakes in Nankai, Japan have also been found to trigger tremor (Han *et al.*, 2014 [29]). I intend to verify whether a similar pattern can be observed for LFEs.

Are there differences or similarities with the San Andreas Fault, and Washington State? I intend to study how the behavior of the LFE families identified by Plourde *et al.* (2015 [52]) on the two strike-slip faults is similar or different from the behavior of the LFE families located on the southern Cascadia Subduction Zone. In particular, I would like to verify whether the LFE families located on the Maacama and Bucknell Creek fault have a similar behavior to what was observed by Shelly (2017 [60]) on the San Andreas Fault, and whether the LFE families located on the southern Cascadia Subduction Zone have a similar behavior to what was observed by Sweet *et al.* (2019 [64]) on the northern Cascadia Subduction Zone.

Once I have obtained the new several-year-long catalog of LFEs, I intend to carry out a more thorough statistical analysis of the occurrence of LFE events. Specifically, I will study how some statistical features of LFE catalogs compare to statistical features of regular earthquake catalogs. It has been shown that whereas the frequency distribution of the magnitude of regular earthquakes follows a power law with b-value ~ 1, the frequency distribution of the magnitude of LFEs follows either a power law with a higher b-value (~ 5, Bostock *et al.*, 2015 [10]) or an exponential law (Sweet *et al.*, 2014 [63]; Chestler and Creager, 2017a [12]). I would like to verify whether LFE catalogs and regular earthquake catalogs differ for other statistical features as well. I will explore two problems:

Long-range dependence (or self-similarity) Long-range dependence is a phenomenon that may arise in the statistical analysis of time series data. It relates to the slow rate of decay of the statistical dependence between two points with increasing time interval between the points. Evidence of long-range dependence has been found in regional earthquakes catalogs (Telesca *et al.*, 2000 [67]; Li *et al.*, 2002 [39]; Telesca *et al.*, 2004 [69]; Enescu *et al.*, 2006 [16]; Jimenez *et al.*, 2006 [34]; Xu and Burton, 2006 [80]; Bunde and Lennartz, 2012 [11]; Wang, 2013 [76]; Gkarlaouni *et al.*, 2017 [26]; Telesca *et al.*, 2017 [68]; Barani *et al.*, 2018 [6]; Matcharashvili *et al.*, 2018 [41]; Mukhopadhyay and Sengupta, 2018 [43]), global earthquakes catalogs (Ogata and Abe, 1991 [48]; Sarlis *et al.*, 2018) [59], and in catalogs of mining-induced seismicity (Węglarczyk and Lasocki, 2009 [79]). We can investigate whether there is long-range dependence in a catalog by computing the fractional index d, which represents how fast the variance in the number of

LFEs in a time window of a given length increases with the length of the time window considered. A fractional index such that $0 < d < 0.5$ is characteristic of long-range dependence in the time series, whereas an homogeneous Poisson process has a fractional index equal to 0. Frank *et al.* (2016 [21]) carried out a statistical analysis of a catalog of LFEs recorded between January 2005 and April 2007 in the Guerrero, Mexico, subduction zone. They computed the autocorrelation sequence and the spectral density function of the LFE event rate for two 4-month-long windows, one corresponding to an inter-slow slip period, and one corresponding to the 2006 slow slip event. They observed that LFEs behave as an homogeneous Poisson's process during the inter-slow slip period, and as a process with long range dependence during the co-slow slip period. I intend to compute the fractional index for all the families in the new two-year-long LFE catalog for southern Cascadia, and compare it to the fractional index obtained for catalogs in Mexico (Frank *et al.*, 2014 [22]), the San Andreas Fault (Shelly, 2017 [60]), and Washington State (Sweet *et al.*, 2019 [64] and Chestler and Creager, 2017a [12] and b [13]).

This kind of statistical analysis may help explain the mechanism producing LFEs. If slow slip produces an increase of the loading rate on the LFE asperities, it should increase the rate of LFEs, but their distribution should still follow a Poisson process. If the fractional index d is higher than 0, it would seem to imply that the occurrence of LFEs does not follow a Poisson process, and that the density of asperities increases during a slow slip event (Frank *et al.*, 2016 [21]). A possible explanation is that a large number of asperities are locked during the inter-slip period, and are activated during slow slip by a mechanism such as migrating pore pressure pulses (Frank *et al.*, 2015 [19]), or along-fault hydrofracturing similar to what is geologically observed on ancient subduction zones (Angiboust *et al.*, 2015 [2]).

Temporal models of seismicity Temporal models of seismicity have been developed to describe, analyze and forecast the probabilities of regular earthquake occurrences. The Epidemic-Type Aftershock Sequence (ETAS) model was first introduced by Ogata (1988 [47]). It takes account the magnitude frequency distribution law of Gutemberg and Richter (1944 [28]) and the Omori-Utsu law of aftershock decay (Omori, 1894 [49]; Utsu, 1957 [72]), but it allows each event, irrespective of whether it is a small or a big event, to trigger its own offspring. According to the Omori-Utsu formula, the number of aftershocks after a mainshock decays as $1/t^p$, where t is the time from the occurrence of the main shock, and the decay rate p can vary between 0.9 and 1.5 (Utsu *et al.*, 1995 [73]). I intend to first verify whether I can fit an ETAS model to the available LFE catalogs, and then verify whether the decay rate for LFE catalogs is similar to the decay rate obtained for regular earthquake catalogs.

The value of the decay rate p is related to the rate-and-state dependent friction law. Dieterich (2007, [15]) has derived an analytical solution for a simplified model of earthquake nucleation where a fault patch of fixed length represents the source. Combining the solutions for earthquake nucleation, and the rate-and-state dependent friction law, he obtained a formulation for the earthquake rate after a step-like change of stress that is similar to the Omori's aftershock decay law with $p = 1$. The variations of the value of p observed in aftershock data could be reproduced by taking into account the heterogeneity of stress change.

Completed work

Extension of the LFE catalog Alexandre Plourde has kindly accepted to share his LFE catalog with me. For each LFE family, each seismic station, and each channel (two horizontal and one vertical), I have downloaded a one-minute-long time window of seismic data around the detection time of each LFE. I have then linearly stacked the data to obtain a template for each LFE family, each seismic station, and each channel. I then used a matched-filter algorithm. To detect new LFEs for a given LFE family, I download one hour of seismic data. Then for each station and each channel, I cross-correlate the one-hour long signal with the one-minute-long template for the given station and channel. As the signal-to-noise ratio of the seismic data is low, we may not see obvious peaks in the cross-correlation signal. However, if we stack the cross-correlation signals for all the channels and all the stations, we can see peaks appearing. Whenever the value of the average cross-correlation is higher than a threshold (generally eight times the median absolute deviation), I assume that there is an LFE.

I first applied the matched-filter algorithm on the time period covered by the catalog of Plourde *et al.* (2015 [52]), and compared the LFE detection times I obtained to the detection times in the original catalog. I have successfully detected nearly all the LFE events that were present in the original catalog and added a few new LFEs (see Table 1 for an example for family 080421.14.048). I missed only two LFEs, but one of them was preceded by another LFE 1.95 seconds before, and the other one was followed by another LFE 3.375 seconds later. In the catalog by Plourde *et al.* (2015 [52]), these LFEs were considered as separate LFEs, but it is possible that the peaks in the cross correlation correspond in fact to the same LFE. I added 13 LFEs to the catalog but they all have a small cross correlation value compared to the other LFEs in the catalog, and they may be false detections. I have reproduced the detection times with similar accuracy for all the LFE families in the original catalog.

I have then used the matched-filter algorithm to extend the catalog to the period 2007-2009 using first both the FAME stations and the permanent stations, and then only the permanent stations (Figure 4), for two different LFE families, one located on the southern Cascadia Subduction Zone (family 080421.14.048), and one located on a strike-slip fault from the San Andreas Fault system (family 080326.08.015). For the subduction zone family, I was able to detect the burst of LFEs during the April 2008 ETS event even when I used only the templates from the permanent stations. The results are more contrasted for the strike-slip fault family. I was able to detect most of the main bursts of LFEs when I used only the templates from the permanent stations, but I missed a few bursts of LFEs. This may be because I have only two seismic stations with three components, and five seismic stations with only the vertical component. Due to the reduced number of channels available, I have more false detections. The stations from the permanent networks have been recording seismic data from at least 2007 until now, and I infer that I will be able to extend the catalog from 2009 to 2019 using only seismic data from the permanent stations.

Statistical analysis of LFE catalogs I have analyzed catalogs of LFEs from Mexico (Frank *et al.*, 2014 [22]), the San Andreas Fault (Shelly, 2017 [60]), and Washington State (Sweet *et al.*, 2019 [64] and Chestler and Creager, 2017a [12] and b [13]). I also analyzed the original LFE catalog of Plourde *et al.* (2015 [52]). For each family of LFEs, I translated the catalog into a

continuous time series defined by number of events per minute. The sample interval is 1 minute. Then, I computed the value of the fractional parameter d, which represents how fast the variance in the number of LFEs increases with the length of the time window considered. Following Taqqu and Teverovsky (1998 [66]), I computed this parameter using the absolute value method, the variance method, the variance of residuals method, the R/S method, and the periodogram method. These methods gave values of d that are consistent between one method and another, except for the absolute value method, and the R/S method. These may be because these methods assume that the time series is stationary, which may not be the case if the time period studied is too short and only one burst of LFEs during a big ETS event has been recorded. The results of the computation of the fractional parameter with the variance method for the four regional areas considered are shown in Figures 5 to 8. For most families of the catalogs studied, I found that $0 < d < 0.5$, which is characteristic of long-range dependence in the time series. On the contrary, $d = 0$ is characteristic of short-range dependence. The only exception is the San Andreas Fault catalog, where the LFE families show a wider range of behaviors, and where only some of the families exhibit evidence for long-range dependence.

Future work

Extension of the LFE catalog I will first use the templates to extend the LFE catalog by Plourde *et al.* (2015) to the period 2007-2009 for all the LFE families in the catalog, as I have already done for two LFE families. Then for each LFE family, I will choose about one hundred LFEs with the best values of the cross correlation coefficient to compute templates for nearby (within a hundred kilometers) permanent stations that were recording during the 2007-2009 period. I will then use these new templates to find LFEs during the same period, and I will compare the catalog computed with the temporary stations from the FAME network and the catalog computed with the permanent stations. If for a given family, I can retrieve most of the LFEs detected with the temporary FAME network when I use only the permanent stations, I will then extend the LFE catalog to the period 2009-2019.

I will then study how low-frequency earthquakes event rate is affected by nearby earthquakes. I will take several moderate earthquakes that occurred near the Mendocino Triple Junction, and test whether there is a change in the LFE event rate before and after the earthquakes. I intend particularly to test the effects of the M5.4 April 30th 2008 earthquake, and the M6.5 January 10th 2010 earthquake. Shelly (2017 [60]) noticed changed in the LFE event rate for some LFE families for at least several months after the M6.0 2004 Parkfield earthquake on the San Andreas Fault. I will also compare the behavior of the most updip LFE families with the behavior of the most downdip LFE families, and verify whether the downdip families are more frequently active than the updip families, as observed by Sweet *et al.* (2019 [64]) in Washington State.

Statistical analysis of LFE catalogs Once I have obtained a two-year-long LFE catalog, I will recompute the value of the fractional parameter for all the LFE families, as I have already done for the two-month-long catalog by Plourde *et al.* (2015 [52]), and I will verify if I still observe evidence for long-range dependence. It is possible that some LFE families follow an homogeneous Poisson process, but still have a small non zero value of the fractional parameter because of the lack of precision of the method used to characterize the long range dependence. I will also try to

quantify the uncertainty on the value of the fractional parameter. I will then try to fit an ETAS model on the available LFE catalogs. I will start with the catalog by Chestler and Creager (2017a [12] and b [13]) because it provides values for the magnitudes of the LFEs. However, it should be possible to fit an ETAS model with the other catalogs as well, by assuming that all the LFEs have the same magnitude, or by looking at the amplitude of the seismic waveforms instead of the magnitude. I intend to use the software R and two available R packages, bayesianETAS by Gordon Ross [54], and PtProcess by David Harte [30].

2.3 Detection of slow slip events in New Zealand

Can we detect smaller and / or longer slow slip events in the absence of spatially and temporally correlated tectonic tremor?

Motivation

As ordinary earthquakes, slow slip events are caused by slip on a fault such as the plate boundary between a tectonic plate subducting under another tectonic plate. However, they take a much longer time (several days to several years) to happen relative to ordinary earthquakes, and the seismic waves they generate are much weaker than the seismic waves generated by ordinary earthquakes, and may not be detectable. A slow slip event on the plate boundary is inferred to happen when there is a reversal of the direction of motion at GPS stations, compared to the secular motion of the surface displacement. Slow slip events have been observed in many subduction zones, such as Cascadia, Nankai (southwest Japan), Alaska, Costa Rica, Mexico, and New Zealand (Beroza and Ide, 2011 [8]; Audet and Kim, 2016 [5]).

In many places, tectonic tremor are also observed in relation to slow slip. In subduction zones such as Nankai and Cascadia, tectonic tremor observations are spatially and temporally correlated with slow slip observations (Obara, 2002 [46]; Rogers and Dragert, 2003 [53]). Due to this correlation, these paired phenomena have been called Episodic Tremor and Slip (ETS). However, this is not always the case. For instance, in northern New Zealand, tremor are more challenging to detect, and seem to be located downdip of the slow slip on the plate boundary.

New Zealand exhibits a wide range of slow slip behavior, and is therefore an exciting site for research. The tectonics of the North Island of New Zealand is dominated by the westward subduction of the Pacific Plate under the Australian Plate at the Hikurangi Trench. Two types of slow slip events have been observed at the Hikurangi margin. Shallow (10-15 km depth), shorter (1-3 weeks), and usually smaller (Mw 6.3-6.8) slow slip events have been observed every 18-24 months in the northern part of the margin. Deeper (35-60 km depth), longer (12-18 months), and larger (Mw 7.0) slow slip events have been observed every 5 years in the southern part of the margin (Wallace and Beavan, 2010 [74]; Todd and Schwartz, 2016 [71]).

It used to be thought that there was no tremor associated with slow slip events in northern Hikurangi. Delahaye *et al.* (2009 [14]) observed an increase in the rate of microseismicity downdip of the 2004 Gisborne slow slip event. More recently however, Kim *et al.* (2011 [37]) detected a low level of tremor activity that increased during the 2010 Gisborne slow slip event. As was

the case for the microearthquakes, the source of the tremor was located downdip of the slow slip patch determined from GPS data. Ide (2012 [32]) detected tremor downdip of the location of two deep slow slip events observed by Wallace and Eberhart-Phillips (2013 [75]) in 2006 and 2008. However, contrary to Episodic Tremor and Slip (ETS) events in Cascadia and Nankai, the tremor activity did not seem to increase during the slow slip events. Todd and Schwartz (2016 [71]) detected tremor associated with most of the shallow slow slip events between 2010 and 2015, and located downdip of the geodetically inferred slip area. They also detected deeper tremor between 20 and 50 km depth with unclear origin. They hypothesized that these tremor may be related to currently undetected deep long-term slow slip events.

In other subduction zones, tremor has been used as a proxy to study slow slip events. For instance, Aguiar *et al.* (2009 [1]) used the tremor occurrence rate to determine the moment released by short tremor episodes for which no slow slip is detectable in the GPS data. Frank (2016 [20]) stacked independently the displacement observed on GPS data during time periods when low-frequency earthquakes are detected, and the displacement observed during time periods when no low-frequency earthquake is detected, and succeeded in observing surface deformation previously hidden in GPS noise. However, as there is no clear relationship between tremor and slow slip occurrence in New Zealand, these methods cannot be applied, and we need other methods to be able to better detect and quantify slow slip.

Several questions could be explored regarding slow slip in northern New Zealand:

Detecting smaller, currently undetected slow slip events. This would help us to verify whether the fault weakens with depth. Indeed, it has been observed in Cascadia that, with decreasing depth, there is a gradation from frequent tremor episodes with small spatial and temporal extent, to infrequent tremor episodes with large spatial and temporal extent (Wech and Creager, 2011 [78]). The same behavior was observed for low-frequency earthquakes (LFEs) with downdip LFEs swarms happening nearly weekly and updip families only occurring during the yearly ETS events (Sweet *et al.*, 2019 [64]). As there is a temporal and spatial correlation between slow slip, tremor and LFEs, the same spatial pattern is also expected for the slow slip. However, the limited resolution of geodetic instruments only allows us to observe the largest slow slip events, and many smaller slow slip events may be undetected. It has been hypothesized that stable sliding at depth transfers stress to the base of the ETS zone, initiating frequent tremor and small slow slip. In a self-similar process, stress is then transferred updip of the fault, triggering less frequent tremor and larger slow slip, up toward the locked zone. This unobserved updip slip could help mediate plate convergence and either lower the slip deficit available for co-seismic slip or shift the downward extent of the megathrust rupture away from urban centers (Wech and Creager, 2011 [78]). Similarly, smaller slow slip events may exist in New Zealand. However, without a good spatiotemporal correlation with tremor occurrence, they are even harder to detect.

Detecting longer term slow slip events. Long term slow slip events have been detected in Japan, Mexico, Alaska, and possibly Cascadia (Nuyen and Schmidt, 2017 [45]). Todd and Schwartz (2016 [71]) detected deep tremor between 20 and 50 km depth with unclear origin and hypothesized that these tremor may be related to deep long-term slow slip events, but were unable to

detect them. Indeed, as a long-term slow slip event releases the same seismic moment at the plate boundary during months (or years) as what is released in a few weeks by a short-term slow slip event, we cannot see a sharp jump in the ground displacement time series, but a slow increase that is harder to detect.

Better measuring of the vertical displacement at the Earth's surface during slow slip events. This is necessary to better constrain the depth extent of the slip area at the plate boundary. The updip limit of the slow slip area is assumed to be one of the constraints on the downdip limit of the megathrust earthquake rupture, a variable that is currently being used in Cascadia for seismic hazard studies, and the design of building codes. Constraining the downdip limit of slow slip is also useful to estimate the area that slips during a slow-motion earthquake, and thus the percentage of the plate convergence that is released by large slow slip episodes. Additionally, the updip and downdip limits of slow slip can be correlated with other geophysical data, such as porosity, temperature, and structure, in an effort to better understand the underlying processes that facilitate aseismic slip. The vertical component of the ground displacement is the most useful in constraining the updip and downdip extent of slip since the sense of motion (uplift versus subsidence) changes for slip at different depths (Szeliga *et al.*, 2008 [65]). However, the vertical displacement is smaller than the horizontal displacement, and generally hard to resolve.

Completed work

I am using data made publicly available by GeoNet, which is a partnership between the Earthquake Commission of New Zealand, GNS Science, and Land Information New Zealand. Ground deformation data are collected continuously by GeoNet using Global Navigation Satellite System (GNSS) receivers and antennas. Daily time series solutions can be easily obtained from GeoNet's website. The coordinates and their formal uncertainties are extracted during the GLOBK run from the combined daily solution files, and converted to (east, north, up) displacement in millimeters with respect to an a priori position and epoch in the ITRF2008 realisation. The resulting time series have no adjustments made to them, so they may, for example, contain offsets due to earthquakes, offsets due to equipment changes at individual sites, and seasonal (annual and semi-annual) signals due to various causes.

I have started to develop a Python library implementing wavelet methods for time series analysis. The Discrete Wavelet Transform (DWT), and its alternative the Maximal Overlap Discrete Wavelet Transform (MODWT), transform a time series X_t into a series of vectors of wavelet coefficients W_j ($j = 1, ..., J$), where J is the level of the wavelet decomposition (Percival and Walden, 2000 [51]). Each wavelet vector W_j is associated with changes on scale $\tau_j = dt2^{j-1}$, where dt is the time step of the time series, and corresponds to the filtering of the original time series with a filter with nominal frequency interval $[\frac{1}{dt2^{j+1}}; \frac{1}{dt2^j}]$. The scaling vector V_J is associated with averages in scale $\lambda_J = dt2^J$, and corresponds to the filtering of the original time series with a filter with nominal frequency interval $[0; \frac{1}{dt2^{J+1}}]$. Using the wavelet coefficients, we can compute the jth wavelet detail D_j and the Jth wavelet smooth S_J. Together, the details and the smooth define the multiresolution analysis (MRA) of X: $X = \sum_{j=1}^{J} D_j + S_J$. The main advantage of the MODWT over the DWT is that when we circularly shift the time series, the corresponding wavelet vectors, scaling vector, details and smooth are shifted by the same amount. Moreover, the details and the

smooth are associated with a zero phase filter, making it easy to meaningfully line up the features of the MRA with the original time series.

As an example, I have carried out the MODWT and the MRA for the eastern component of the time series recorded at five stations in the Northern Island of New Zealand (PUKE, ANAU, GISB, MAHI, and CKID). The 6^{th} level detail for each station is plotted in Figure 9. It corresponds to changes on scale 64 days, which is about twice the duration of a slow slip event. The grey bars show the time of the transients listed by Todd and Schwartz (2016 [71], their Table 1). For station CKID, all the peaks observed in the 6^{th} level detail between 2010 and 2015 correspond to a slow slip event. For stations GISB and MAHI, the main peaks observed in the 6^{th} level detail between 2010 and 2015 correspond to a slow slip event. However, not all slow slip events are associated with peaks in the 6^{th} level detail. It may be because they have a shorter duration (and thus should be seen on a lower level detail), or are too close to each other. Slow slip events are less obvious for stations ANAU and PUKE, maybe because they happen very closely to each other.

An important application of the DWT and the MODWT is the estimation of a signal hidden by noise within an observed time series. The main idea is to modify the elements of the wavelet vectors W_j, to produce new wavelet vectors W_j' from which an estimate of the signal can be synthesized using the inverse wavelet transform. The wavelet vectors can be transformed using thresholding, scaling, or shrinkage (Percival and Walden, 2000 [51]). As an example, Figure 10 shows a synthetic time series with slow slip events of durations 20 and 50 days, to which a Gaussian noise has been added, the corresponding denoised signal obtained using thresholding of the wavelet vectors, and the signal obtained with a low-pass filter. Although the signal is barely visible behind the noise in the left-hand panel with duration 20 days and signal-to-noise ratio 1, we can see in the denoised signal that there is a unique ramp-like signal in the data, whereas the low-pass filtered signal shows several ramp-like features.

I have applied this denoising method to GPS time series. Figure 11 shows the denoised time series obtained applying the thresholding method to the eastern and the vertical components of the displacement at GPS station CKID, located in the North Island of New Zealand. The denoising and the low-pass filtering give similar results for the horizontal component, but the denoising highlights different features for the vertical component.

Future work

Detecting smaller, currently undetected slow slip events. I intend to combine MRA of several channels and several stations, and stack them with some time shift to take into account a possible propagation of the slow slip event along the plate boundary, in order to get a better wavelet signal, and be able to see peaks in the wavelet details currently unseen. Another possibility is to use a matching pursuit algorithm. The idea is to approximate the time series by a small number of basis wavelet vectors (Mallat and Zhang, 1993 [40]) in order to obtain an adaptive time / frequency decomposition of the time series by using a sum of waveforms whose localizations in time and frequency match those of pertinent structures in the time series (Percival and Walden, 2000 [51]). Regarding this research problem, I expect that the first wavelet basis vectors obtained with the matching pursuit algorithm will correspond to the biggest slow slip events, but that some

other wavelet basis vectors that could be associated with smaller events will also appear in the decomposition.

Detecting longer term slow slip events. I expect that longer term slow slip events could be seen on the wavelet details at larger scale. However, computing these details at larger scale requires having a continuous time series. Currently, there are some missing data in the GPS recordings due to instrumental dysfunction. I intend to replace the missing data points by synthetic data points obtained by a combination of linear or more complex interpolation and random Gaussian noise. To verify whether the method chosen to deal with missing data points could affect the results of the wavelet analysis, I will test the method on the GPS stations where long time series without missing data are available. I will remove one or more existing points, replace them using different interpolation methods, and compare the MRA obtained with the original points and the interpolated points.

Better measuring of the vertical displacement at the Earth's surface during slow slip events. I intend to use wavelet-based methods to denoise the time series, by applying thresholding, scaling, or shrinkage of the wavelet coefficients before reconstructing the time series using the inverse wavelet transform. I will test several denoising methods. If one of them improve the accuracy of the measurement of the vertical displacement during a slow slip event, the results may be used to carry out inversions of slow slip events, and obtained the slip history of the fault at depth.

3 Timeline

Time	PhD Work	Other Activities
Fall 2019	General exam	Present slow slip work at AGU Fall Meeting
Winter 2020	Write paper on tremor in northern Cascadia	
Spring 2020	Write paper on LFE catalogs in southern Cascadia	Present work on LFEs at SIAM Conference on Mathematics of Data Science
Summer 2020		
Fall 2020	Write paper on statistical analysis of LFE catalog	
Winter 2021		
Spring 2021	Write paper on wavelet analysis of slow slip	
Summer 2021	Defend by mid-summer	Present work on statistical analysis of LFEs catalog at Workshop on Statistical Seismology

References

[1] A.C. Aguiar, T.I. Melbourne, and C.W. Scrivner. Moment release rate of Cascadia tremor constrained by GPS. *Journal of Geophysical Research*, 114:B00A05, 2009.

[2] S. Angiboust, J. Kirsch, O. Oncken, J. Glodny, P. Monié, and E. Rybacki. Probing the transition between seismically coupled and decoupled segments along an ancient subduction interface. *Geochemistry, Geophysics, Geosystems*, 16:1905–1922, 2015.

[3] P. Audet, M.G. Bostock, N.I. Christensen, and S.M. Peacock. Seismic evidence for overpressured subducted oceanic crust and megathrust fault sealing. *Nature*, 457:76–78, 2009.

[4] P. Audet and R. Bürgmann. Possible control of subduction zone slow-earthquake periodicity by silica enrichment. *Nature*, 510:389–393, 2014.

[5] P. Audet and Y.H. Kim. Teleseismic constraints on the geological environment of deep episodic slow earthquakes in subduction zone forearcs: A review. *Tectonophysics*, 670:1–15, 2016.

[6] S. Barani, C. Mascandola, E. Riccomagno, D. Spallarossa, D. Albarello, G. Ferretti, D. Scafidi, P. Augliera, and M. Massa. Long-range dependence in earthquake-moment release and implications for earthquake occurrence probability. *Scientific Reports*, 8(1):1–11, 2018.

[7] L.-M. Baratin, C.J. Chamberlain, J. Townend, and M.K. Savage. Focal mechanisms and inter-event times of low-frequency earthquakes reveal quasi-continuous deformation and triggered slow slip on the deep Alpine Fault. *Earth and Planetary Science Letters*, 484:111–123, 2018.

[8] G.C. Beroza and S. Ide. Slow earthquakes and nonvolcanic tremor. *Annual Review of Earth and Planetary Sciences*, 39:271–296, 2011.

[9] M.G. Bostock, A.A. Royer, E.H. Hearn, and S.M. Peacock. Low frequency earthquakes below southern Vancouver Island. *Geochemistry Geophysics Geosystems*, 13:Q11007, 2012.

[10] M.G. Bostock, A.M. Thomas, G. Savard, L. Chuang, and A.M. Rubin. Magnitudes and moment-duration scaling of low-frequency earthquakes beneath southern Vancouver Island. *Journal of Geophysical Research Solid Earth*, 120:6329–6350, 2015.

[11] A. Bunde and S. Lennartz. Long-term correlations in Earth sciences. *Acta Geophysica*, 60(3):562–588, 2012.

[12] S.R. Chestler and K.C. Creager. Evidence for a scale-limited low-frequecny earthquake source process. *Journal of Geophysical Research. Solid Earth*, 122:3099–3114, 2017. doi:10.1002/2016jb013717.

[13] S.R. Chestler and K.C. Creager. A model for low-frequency earthquake slip. *Geochemistry, Geophysics, Geosystems*, 18:4690–4708, 2017. doi:10.1002/2017gc007253.

[14] E.J. Delahaye, J. Townend, M.E. Reyners, and G. Rogers. Microseismicity but no tremor accompanying slow slip in the Hikurangi subduction zone, New Zealand. *Earth and Planetary Science Letters*, 277:21–28, 2009.

[15] J.H. Dieterich. *Applications of rate- and state-dependent friction to models of fault slip and earthquake occurrence*, volume 4 of *Treatise on Geophysics*, chapter 4, pages 107–129. Elsevier, 2007.

[16] B. Enescu, K. Ito, and Z.R. Struzik. Wavelet-based multiscale resolution analysis of real and simulated time-series of earthquakes. *Geophysical Journal International*, 64:63–74, 2006.

[17] Å. Fagereng and J.F.A. Diener. Non-volcanic tremor and discontinuous slab dehydration. *Geophysical Research Letters*, 38:L15302, 2011.

[18] Å. Fagereng, Hillary G.W.B., and J.F.A. Diener. Brittle-viscous deformation, slow slip, and tremor. *Geophysical Research Letters*, 41(12):4159–4167, 2014.

[19] W. B. Frank, M. Radiguet, B. Rousset, N.M. Shapiro, A.L. Husker, V. Kostoglodov, N. Cotte, and M. Campillo. Uncovering the geodetic signature of silent slip through repeating earthquakes. *Geophysical Research Letters*, 42:2774–2779, 2015.

[20] W.B. Frank. Slow slip hidden in the noise: The intermittence of tectonic release. *Geophysical Research Letters*, 43:10125–10133, 2016.

[21] W.B. Frank, N.M. Shapiro, A.L. Husker, V. Kostoglodov, A.A. Gusev, and M. Campillo. The evolving interaction of low-frequency earthquakes during transient slip. *Science Advances*, 2:e1501616, 2016.

[22] W.B. Frank, N.M. Shapiro, A.L. Husker, V. Kostoglodov, A. Romanenko, and M. Campillo. Using systematically characterized low-frequency earthquakes as a fault probe in Guerrero, Mexico. *Journal of Geophysical Research Solid Earth*, 119:7686–7700, 2014.

[23] A. Ghosh, J.E. Vidale, and K.C. Creager. Tremor asperities in the transition zone control evolution of slow earthquakes. *Journal of Geophysical Research*, 117:B10301, 2012.

[24] A. Ghosh, J.E. Vidale, J.R. Sweet, K.C. Creager, A.G. Wech, H. Houston, and E.E. Brodsky. Rapid, continuous streaking of tremor in Cascadia. *Geochemistry, Geophysics, Geosystems*, 11:Q12010, 2010.

[25] J.E. Ghosh, A. Vidale, J.R. Sweet, K.C. Creager, A.G. Wech, and H. Houston. Tremor bands sweep Cascadia. *Geophysical Research Letters*, 37:L08301, 2010.

[26] C. Gkarlaouni, S. Lasocki, E. Papadimitriou, and T. George. Hurst analysis of seismicity in Corinth rift and Mygdonia graben (Greece). *Chaos, Solitons and Fractals*, 96:30–42, 2017.

[27] A. Guilhem, Z. Peng, and R.M. Nadeau. High-frequency identification of non-volcanic tremor triggered by regional earthquakes. *Geophysical Research Letters*, 37:L16309, 2010.

[28] B. Gutenberg and C.F. Richter. Frequency of earthquakes in California. *Bulletin of the Seismological Society of America*, 34(4):185–188, 1944.

[29] J. Han, J.E. Vidale, H. Houston, K. Chao, and K. Obara. Triggering of tremor and inferred slow slip by small earthquakes at the Nankai subduction zone in southwest Japan. *Geophysical Research Letters*, 41:8053–8060, 2014.

[30] D. Harte. PtProcess: An R package for modelling marked point processes indexed by time. *Journal of Statistical Software*, 35(8):1–32, 2010.

[31] R.D. Hyndman, P.A. McCrory, A. Wech, H. Kao, and Ague J. Cascadia subducting plate fluids channelled to fore-arc mantle corner: ETS and silica deposition. *Journal of Geophysical Research Solid Earth*, 120:4344–4358, 2015.

[32] S. Ide. Variety and spatial heterogeneity of tectonic tremor worldwide. *Journal of Geophysical Research*, 117:B03302, 2012.

[33] S. Ide, D.R. Shelly, and G.C. Beroza. Mechanism of deep low frequency earthquakes: Further evidence that deep non-volcanic tremor is generated by shear slip on the plate interface. *Geophysical Research Letters*, 34:L03308, 2007.

[34] A. Jiménez, K.F. Tiampo, S. Levin, and A.M. Posadas. Testing the persistence in earthquake catalogs: The Iberian Peninsula. *Europhysics Letters*, 73(2):171–177, 2006.

[35] H. Kao, S.-J. Shan, H. Dragert, and G. Rogers. Northern Cascadia episodic tremor and slip: A decade of tremor observations from 1997 to 2007. *Journal of Geophysical Research*, 114:B00A12, 2009.

[36] H. Kao, S.-J. Shan, H. Dragert, G. Rogers, J.F. Cassidy, K. Wang, T.S. James, and K. Ramachandran. Spatial-temporal patterns of seismic tremors in northern Cascadia. *Journal of Geophysical Research*, 111:B03309, 2006.

[37] M.J. Kim, S.Y. Schwartz, and S. Bannister. Non-volcanic tremor associated with the March 2010 Gisborne slow slip event at the Hikurangi subduction margin, New Zealand. *Geophysical Research Letters*, 38:L14301, 2011.

[38] M. La Rocca, K.C. Creager, D. Galluzzo, S. Malone, J.E. Vidale, J.R. Sweet, and A.G. Wech. Cascadia tremor located near plate interface constrained by S minus P wave times. *Science*, 323:620–623, 2009.

[39] J. Li, Y. Chen, and H. Mi. $1/f^{\beta}$ temporal fluctuation: Detecting scale-invariance properties of seismic activity in North China. *Chaos, Solitons and Fractals*, 14:1487–1494, 2002.

[40] S.G. Mallat and Z. Zhang. Matching pursuits with time-frequency dictionaries. *IEEE Transactions on Signal Processing*, 41:3397–3415, 1993.

[41] T. Matcharashvili, T. Hatano, T. Chelidze, and N. Zhukova. Simple statistics for complex Earthquake time distributions. *Nonlinear Processes in Geophysics*, 25:497–510, 2018.

[42] P.A. McCrory, J.L. Blair, D.H. Oppenheimer, and S.R. Walter. Depth to the Juan de Fuca slab beneath the Cascadia subduction margin - a 3-D model sorting earthquakes. Technical Report Series 91, U.S. Geological Survey, 2006.

[43] B. Mukhopadhyay and D. Sengupta. Seismic moment release data in earthquake catalogue: Application of Hurst statistics in delineating temporal clustering and seismic vulnerability. *Journal Geological Society of India*, 91:15–24, 2018.

[44] R. Nakata, N. Suda, and H. Tsuruoka. Non-volcanic tremor resulting from the combined effect of Earth tides and slow slip events. *Nature Geoscience*, 1:676–678, 2008.

[45] C. Nuyen and D. A. Schmidt. Exploring low-amplitude, long-duration deformational transients on the Cascadia Subduction Zone. In *American Geophysical Union, Fall Meeting*, pages S41C–0790, December 2017.

[46] K. Obara. Nonvolcanic deep tremor associated with subduction in southwest Japan. *Science*, 296(5573):1679–1681, 2002.

[47] Y. Ogata. Statistical models for earthquake occurrences and residual analysis for point processes. *Journal of the American Statistical Association*, 83(401):9–27, 1988.

[48] Y. Ogata and K. Abe. Some statistical features of the long-term variation of the global and regional seismic activity. *International Statistical Review*, 59(2):139–161, 1991.

[49] F. Omori. On the aftershocks of earthquakes. *Journal of the College of Science, Imperial University of Tokyo*, 7:111–200, 1894.

[50] Z. Peng, J.E. Vidale, A.G. Wech, R.M. Nadeau, and K.C. Creager. Remote triggering of tremor along the San Andreas Fault in central California. *Journal of Geophysical Research*, 114:B00A06, 2009.

[51] D.B. Percival and A.T. Walden. *Wavelet Methods for Time Series Analysis*. Cambridge Series in Statistical and Probabilistic Mathematics. Cambridge University Press, New York, NY, USA, 2000.

[52] A.P. Plourde, M.G. Bostock, P. Audet, and A.M. Thomas. Low-frequency earthquakes at the southern Cascadia margin. *Geophysical Research Letters*, 42:4849–4855, 2015. doi:10.1002/2015gl064363.

[53] G. Rogers and H. Dragert. Tremor and slip on the Cascadia subduction zone: The chatter of silent slip. *Science*, 300(5627):1942–1943, 2003.

[54] G.J. Ross. Bayesian estimation of the ETAS model for earthquake occurrences. Available at http://www.gordonjross.co.uk/bayesianetas.pdf, 2016.

[55] C. Rowe and F. Moore, J. Remitti. The thickness of subduction plate boundary faults from the seafloor into the seismogenic zone. *Geology*, 41:991–994, 2013.

[56] A.A. Royer and M.G. Rostock. A comparative study of low frequency earthquake templates in northern Cascadia. *Earth and Planetary Science Letters*, 402:247–256, 2014.

[57] A.M. Rubin and J.G. Armbruster. Imaging slow slip fronts in Cascadia with high precision cross-station tremor locations. *Geochemistry Geophysics Geosystems*, 14:5371–5392, 2013.

[58] J.L. Rubinstein, J. Gomberg, J.E. Vidale, A.G. Wech, H. Kao, K.C. Creager, and G. Rogers. Seismic wave triggering of nonvolcanic tremor, episodic tremor and slip, and earthquakes on Vancouver Island. *Journal of Geophysical Research Solid Earth*, 114:B00A01, 2009.

[59] N. Sarlis, E. Skordas, A. Mintzelas, and K. Papadopoulou. Micro-scale, mid-scale, and macroscale in global seismicity identified by empirical mode decomposition and their multifractal characteristics. *Scientific Reports*, 8:1–15, 2018.

[60] D.R. Shelly. A 15 year catalog of more than 1 million low-frequency earthquakes: Tracking tremor and slip along the deep San Andreas fault. *Journal of Geophysical Research. Solid Earth*, 122:3739–3753, 2017. doi:10.1002/2017jb014047.

[61] D.R. Shelly, G.C. Beroza, and S. Ide. Non-volcanic tremor and low-frequency earthquake swarms. *Nature*, 446:305–307, 2007.

[62] D.R. Shelly, G.C. Beroza, S. Ide, and S. Nakamula. Low-frequency earthquakes in Shikoku, Japan, and their relationship to episodic tremor and slip. *Nature*, 442:188–192, 2006.

[63] J.R. Sweet, K.C. Creager, and H. Houston. A family of repeating low-frequency earthquakes at the downdip edge of tremor and slip. *Geochemistry Geophysics Geosystems*, 15:3713–3721, 2014.

[64] J.R. Sweet, K.C. Creager, H. Houston, and S.R. Chestler. Variations in Cascadia low-frequency earthquake behavior with downdip distance. *Geochemistry, Geophysics, Geosystems*, 20:1202–1217, 2019.

[65] W. Szeliga, T. Melbourne, M. Santillan, and M. Miller. GPS constraints on 34 slow slip events within the Cascadia subduction zone, 1997-2005. *Journal of Geophysical Research*, 113:B04404, 2008.

[66] M. Taqqu and V. Teverovsky. On estimating the intensity of long-range dependence in finite and infinite variance time series. In R.J. Adler, R.E. Feldman, and M.S. Taqqu, editors, *A Practical Guide to Heavy Tails: Statistical Techniques and Application*. Birkhäuser, Boston, MA, USA, 1998.

[67] L. Telesca, V. Cuomo, V. Lapenna, and F. Vallianatos. Self-similarity properties of seismicity in the Southern Aegean area. *Tectonophysics*, 321:179–188, 2000.

[68] L. Telesca, F. Kadirov, G. Yetirmishli, G. Safarov, R. Babayev, and S. Ismaylova. Statistical analysis of the 2003-2016 seismicity of Azerbaijan and surrounding areas. *Journal of Seismology*, 21:14671485, 2017.

[69] L. Telesca, V. Lapenna, and M. Macchiato. Mono- and multi-fractal investigation of scaling properties in temporal patterns of seismic sequences. *Chaos, Solitons and Fractals*, 19:1–15, 2004.

[70] A.M. Thomas, R.M. Nadeau, and R. Bürgmann. Tremor-tide correlations and near-lithostatic pore pressure on the deep San Andreas fault. *Nature*, 462:1048–1051, 2009.

[71] E.K. Todd and S.Y. Schwartz. Tectonic tremor along the northern Hikurangi Margin, New Zealand, between 2010 and 2015. *Journal of Geophysical Research Solid Earth*, 121:8706–8719, 2016.

[72] T Utsu. Magnitude of earthquakes and occurrence of their aftershocks. *Zisin (Journal of the Seismological Society of Japan)*, 10:35–45, 1957.

[73] T. Utsu, Y. Ogata, and R. Matsu'ura. The centenary of the Omori formula for a decay law of aftershock activity. *Journal of Physics of the Earth*, 43:1–33, 1995.

[74] L.M. Wallace and J. Beavan. Diverse slow slip behavior at the Hikurangi subduction margin, New Zealand. *Journal of Geophysical Research*, 115:B12402, 2010.

[75] L.M. Wallace and D. Eberhart-Phillips. Newly observed, deep slow slip events at the central Hikurangi margin, New Zealand: Implications for downdip variability of slow slip and tremor, and relationship to seismic structure. *Geophysical Research Letters*, 40:5393–5398, 2013.

[76] J.-H. Wang. Memory effect in $M \geq 6$ earthquakes of South-North Seismic Belt, Mainland China. *Journal of Seismology*, 17:913–924, 2013.

[77] A.G. Wech and K.C. Creager. Automated detection and location of Cascadia tremor. *Geophysical Research Letters*, 35:L20302, 2008.

[78] A.G. Wech and K.C. Creager. A continuum of stress, strength and slip in the Cascadia subduction zone. *Nature Geoscience*, 4:624–628, 2011.

[79] S. Węglarczyk and S. Lasocki. Studies of short and long memory in mining-induced seismic processes. *Acta Geophysica*, 57:696–715, 2009.

[80] Y. Xu and P.W. Burton. Time varying seismicity in Greece: Hurst's analysis and Monte Carlo simulation applied to a new earthquake catalogue for Greece. *Tectonophysics*, 423:125–136, 2006.

Tables

Number of LFEs in my catalog	236
Number of LFEs in the catalog by Plourde *et al.* (2015 [52])	225
Number of LFEs added in my catalog	13
Number of LFEs missing in my catalog	2
Number of LFEs present in both catalogs	223

Table 1: Comparison between the LFE catalog by Plourde *et al.* (2015 [52]), and my new catalog using templates obtained from their detection times for LFE family 080421.14.048.

Figures

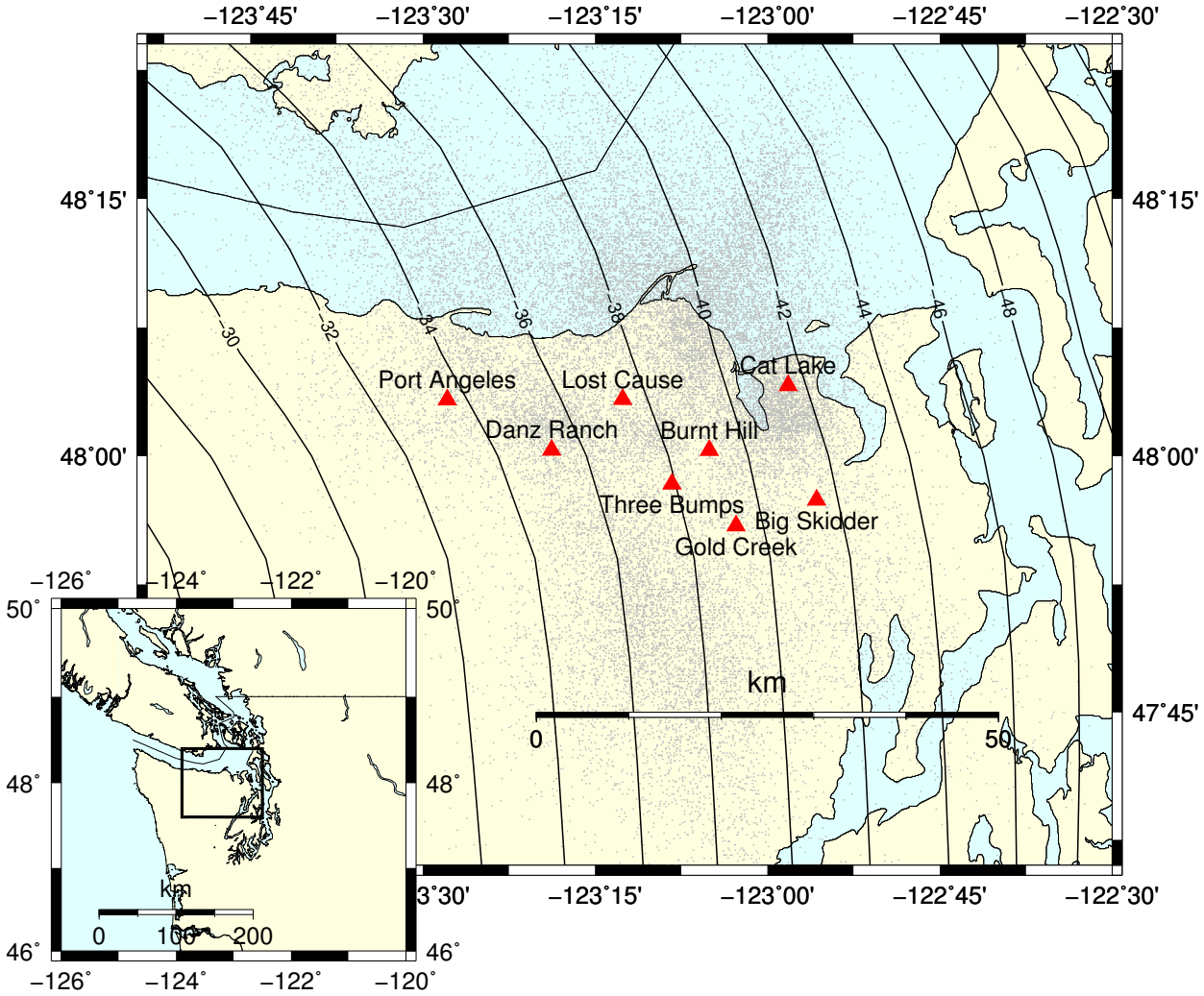

Figure 1: Map showing the location of the eight arrays (red dots) used in this study. Grey dots are the locations of the source of the tremor recorded by the arrays. Inset shows the study area with the box marking the area covered in the main map. Contour lines represent a model of the depth of the plate interface [42].

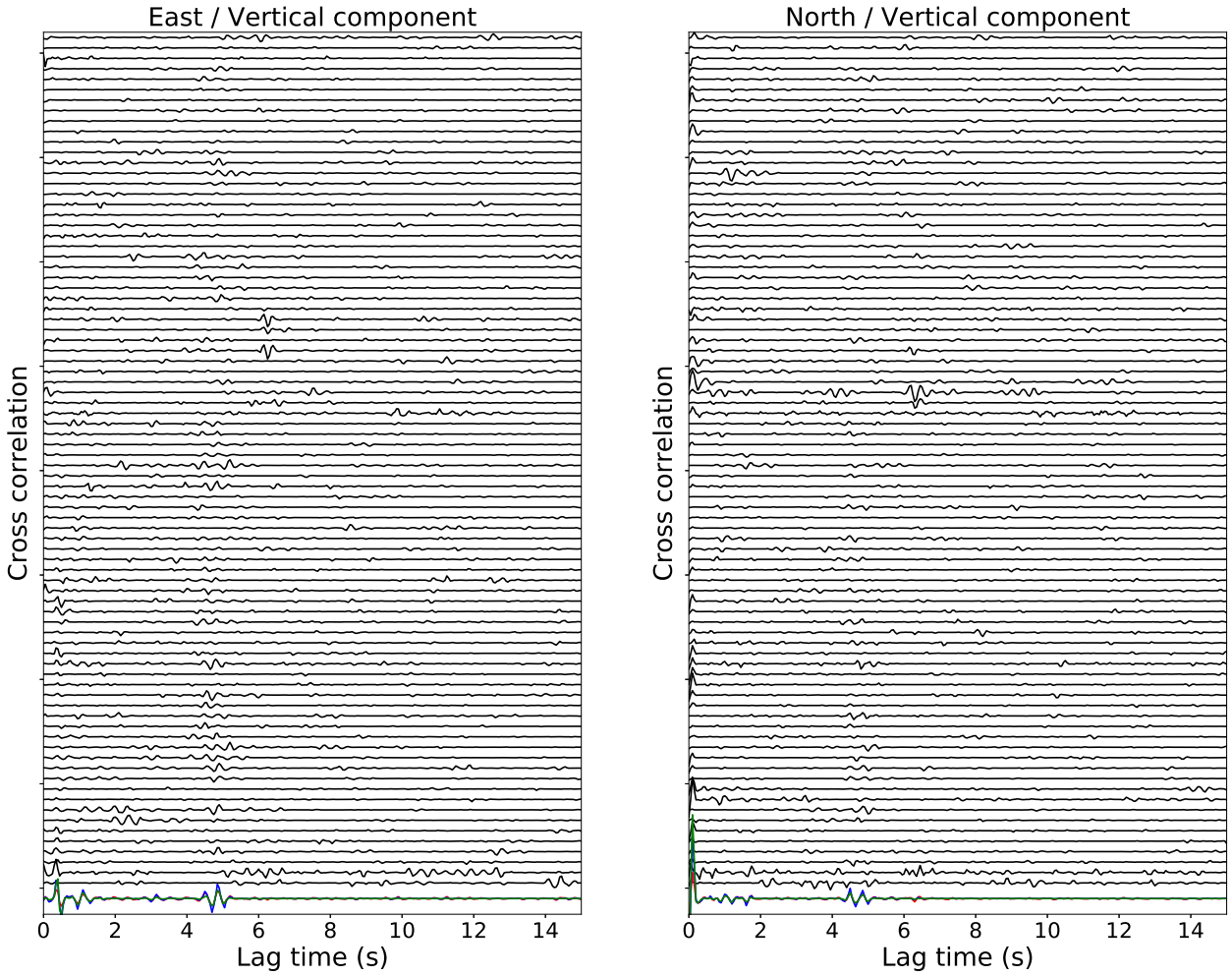

Figure 2: Stacked cross correlation functions as function of time for the Big Skidder array for the 82 one-minute long time windows when tremor was detected in a 5 km by 5 km grid cell centered on the array. We used a phase-weighted stack to stack the cross-correlation functions over all the seismic stations. The colored cross-correlation at the end represent the stack over all the 82 time windows, red is for linear-stack, blue is for n-root stack and green is for phase-weighted stack. Left panel is the cross correlation of the EW component with the vertical component, and right panel is the cross correlation of the NS component with the vertical component.

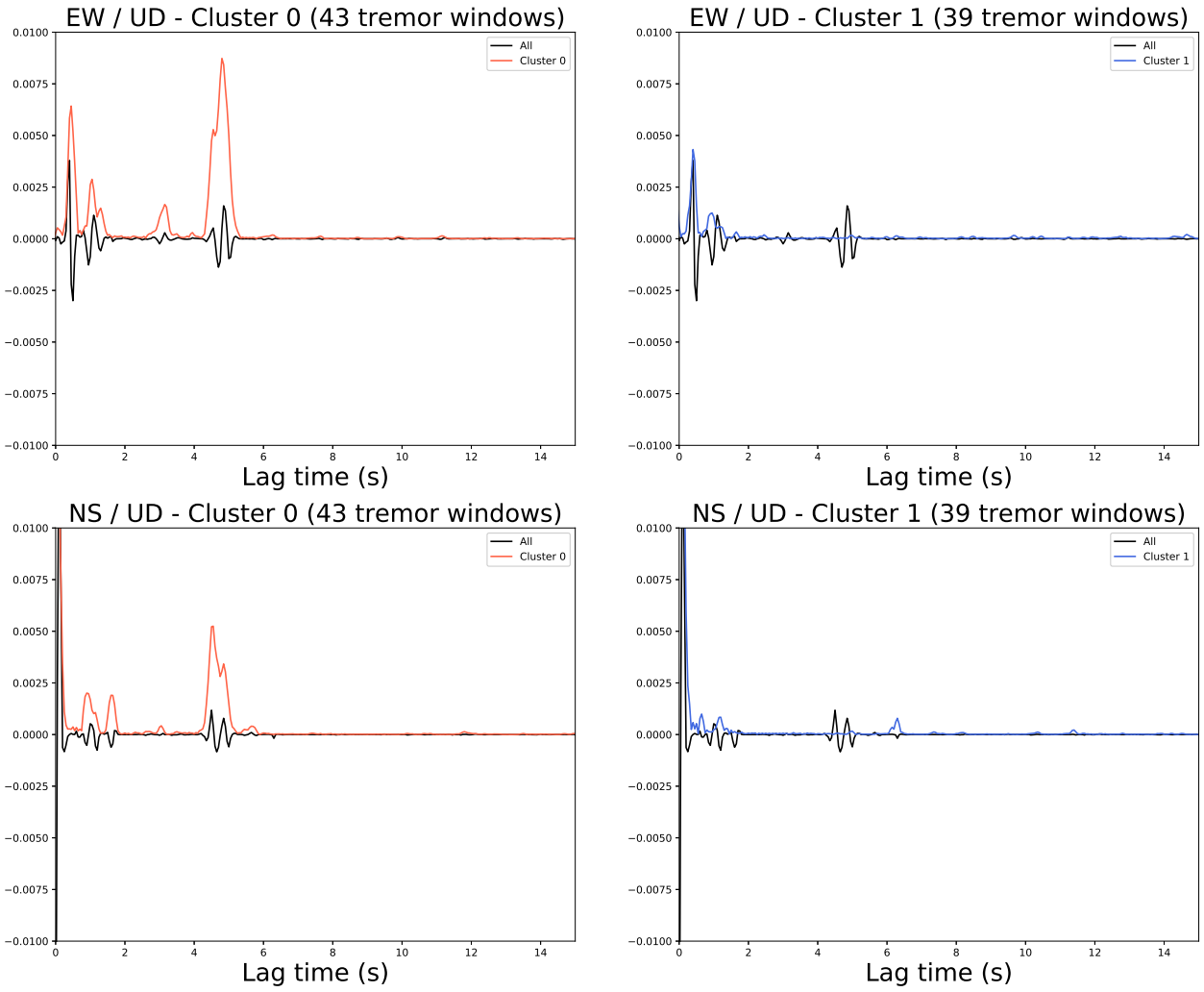

Figure 3: Stack of the cross correlation functions over all the 82 time windows from Figure 2. We used a phase-weighted stack for the stack over the stations and for the stack over the time windows. The black line is the stack over all the time windows. The red line on the left panels is the envelope of the stack over the time windows in the first cluster (which contains the time windows that fit well with the stack), and the blue line on the right panels is the envelope of the stack over the time windows in the second cluster (which contains the time windows that do not fit well with the stack). Top panels are the cross correlation of the EW component with the vertical component, and bottom panels are the cross correlation of the NS component with the vertical component.

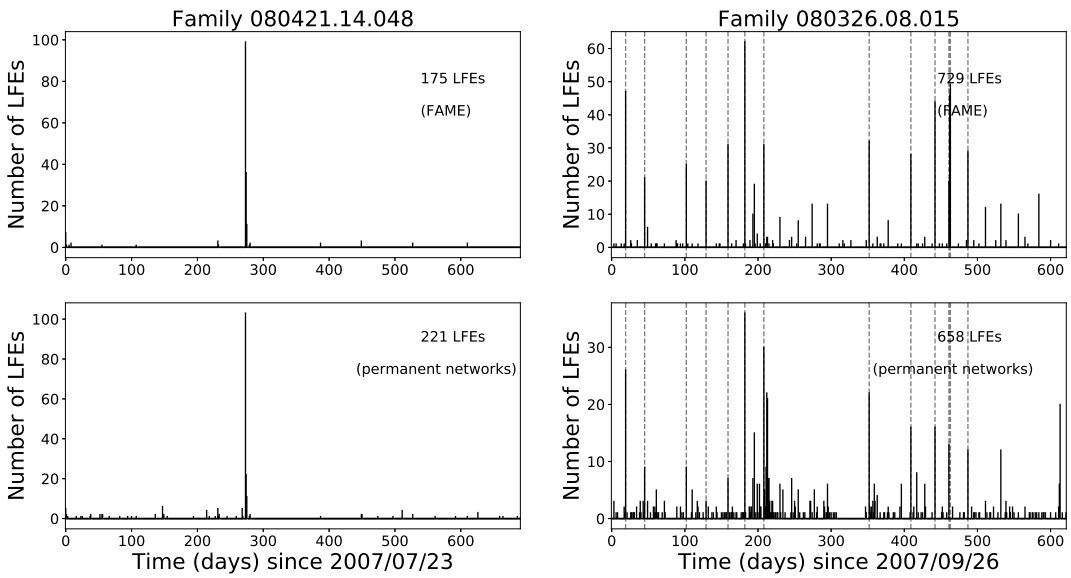

Figure 4: Number of LFEs per day for subduction zone LFE family 080421.14.048 (left) and strike-slip fault family 080326.08.015 (right) detected with the FAME stations (top) and the permanent stations (bottom). The grey dashed lines on the left panels show the timing of the main bursts of LFEs.

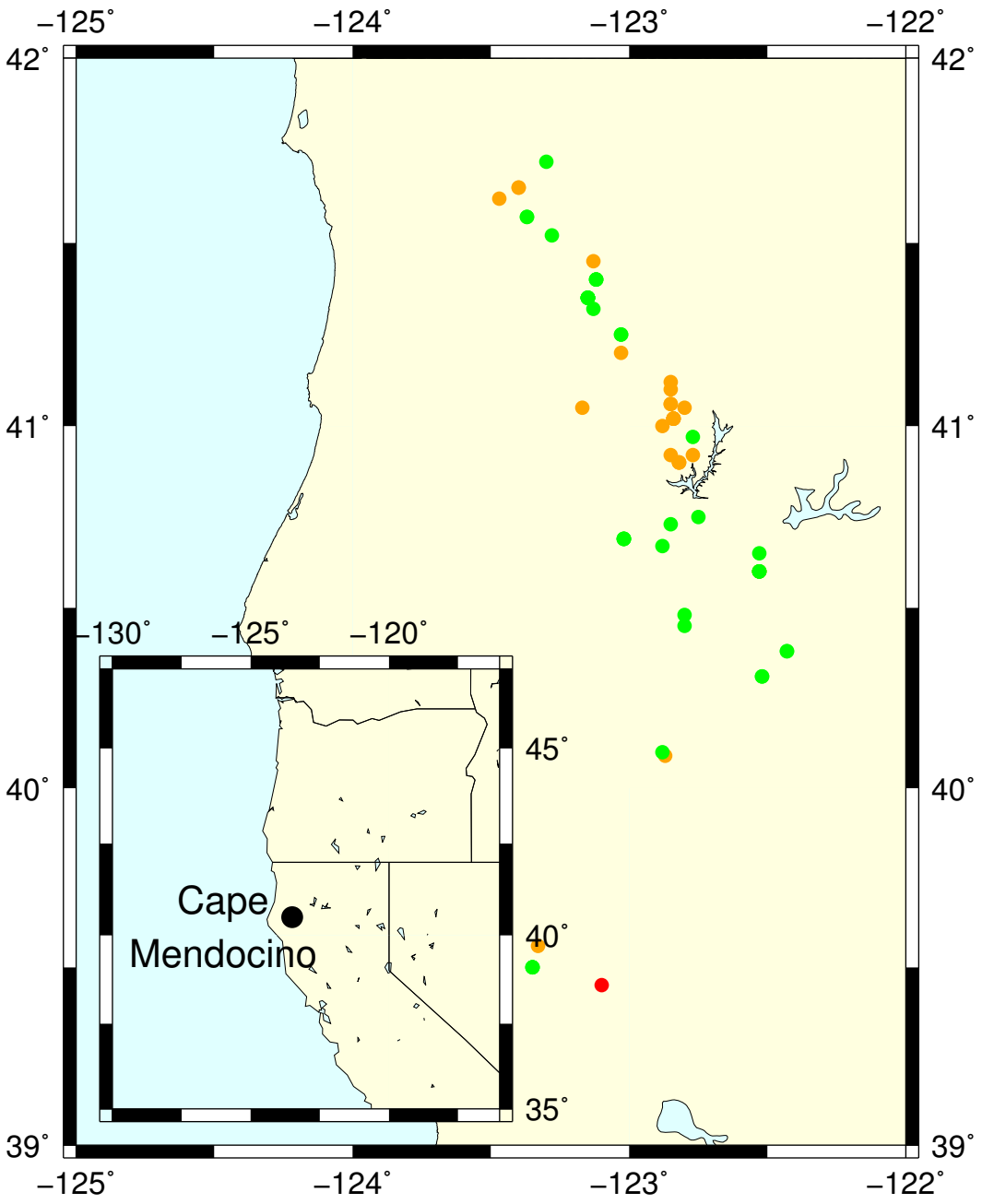

Figure 5: Fractional index for 66 low-frequency earthquakes families in Northern California (catalog by Plourde *et al.* (2015 [52]). Red dots correspond to $0 < d < 0.1$. Orange dots correspond to $0.1 < d < 0.2$. Green dots correspond to $0.2 < d < 0.3$. Cyan dots correspond to $0.3 < d < 0.4$.

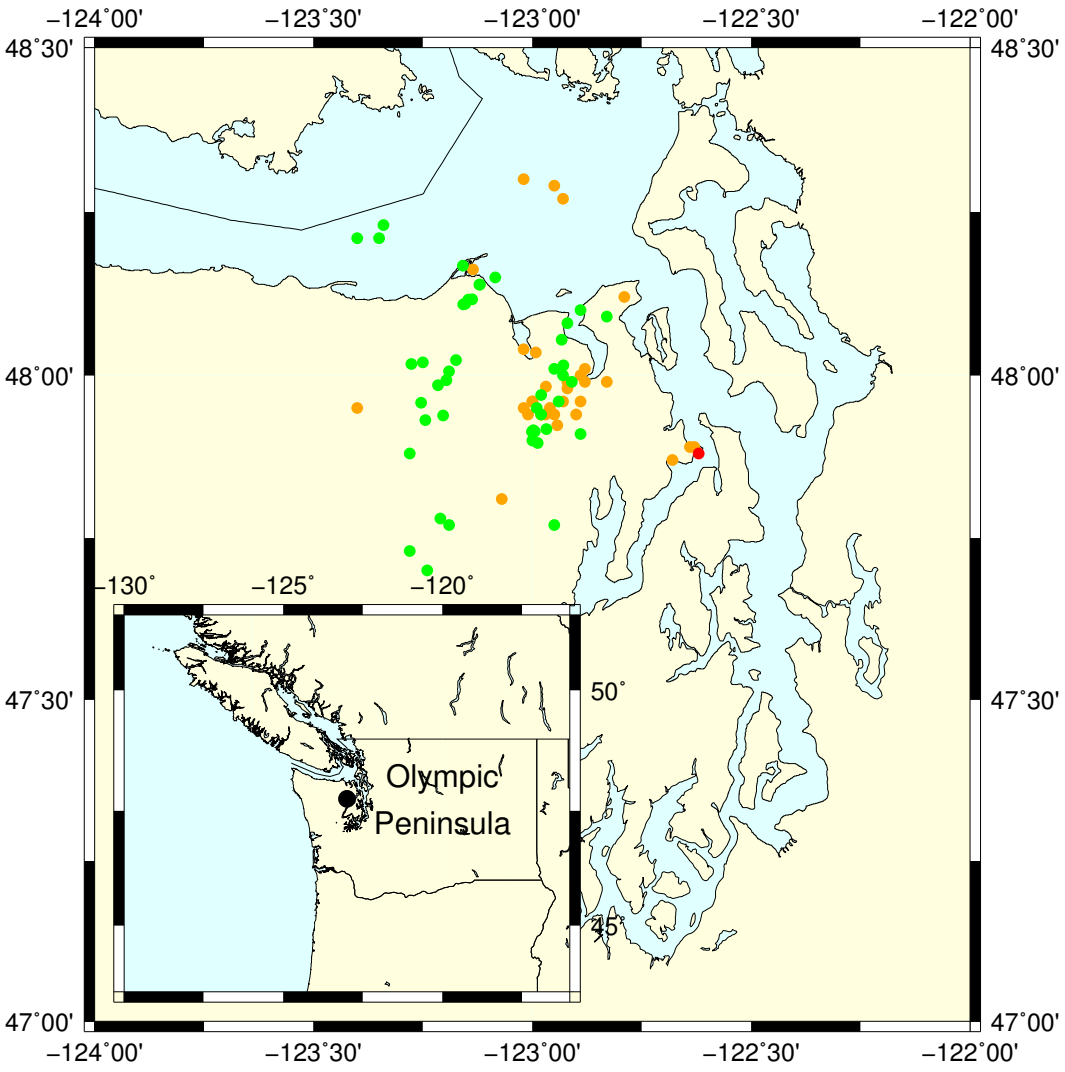

Figure 6: Fractional index for 78 low-frequency earthquakes families in the Olympic Peninsula, Washington (catalogs by Chestler and Creager (2017a [12] and b [13]) and Sweet *et al.* (2019 [64])). Red dots correspond to $0 < d < 0.1$. Orange dots correspond to $0.1 < d < 0.2$. Green dots correspond to $0.2 < d < 0.3$. Cyan dots correspond to $0.3 < d < 0.4$.

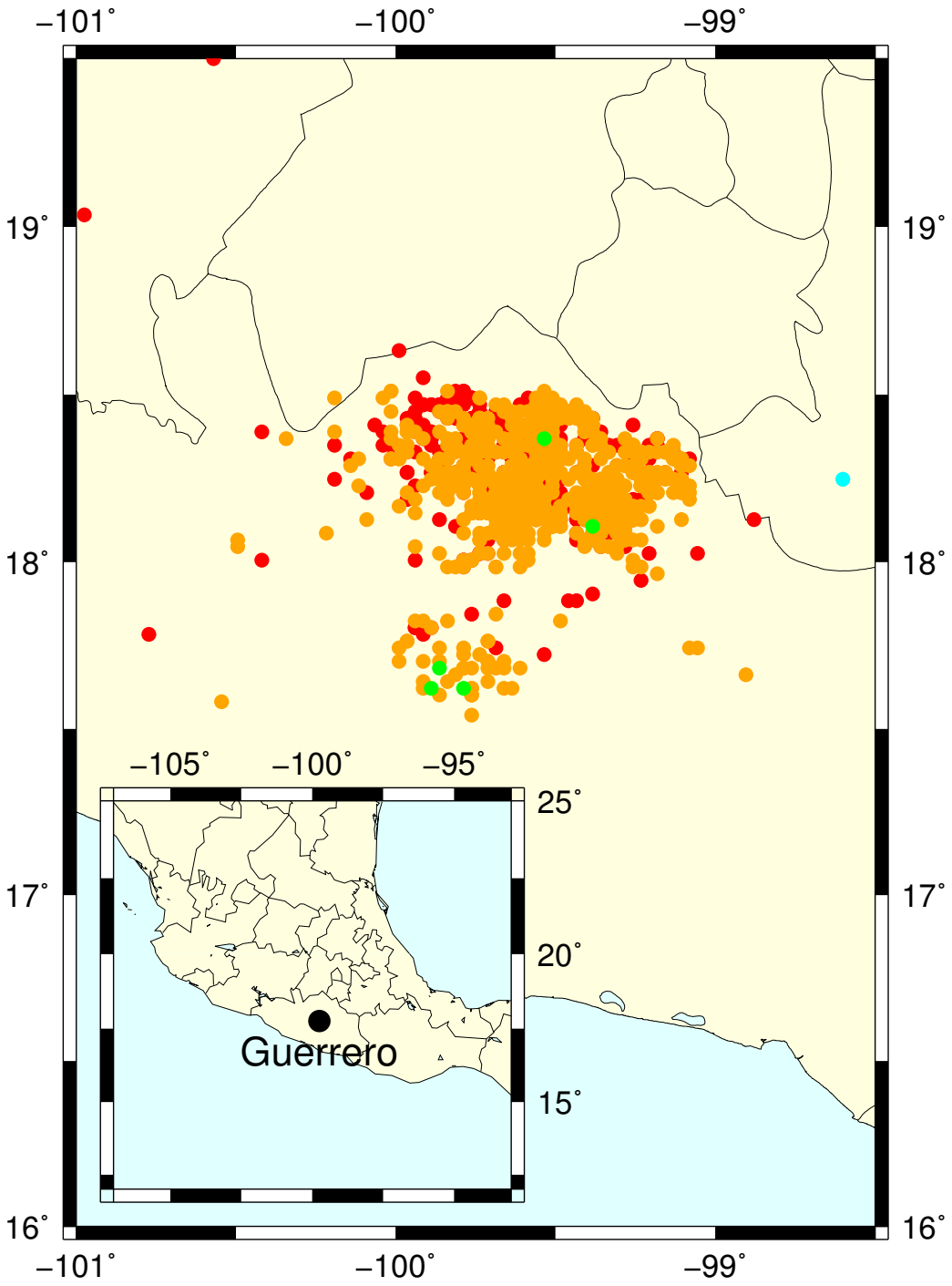

Figure 7: Fractional index for 1120 low-frequency earthquakes families in Guerrero, Mexico (catalog by Frank *et al.* 92016 [21]). Red dots correspond to $0 < d < 0.1$. Orange dots correspond to $0.1 < d < 0.2$. Green dots correspond to $0.2 < d < 0.3$. Cyan dots correspond to $0.3 < d < 0.4$.

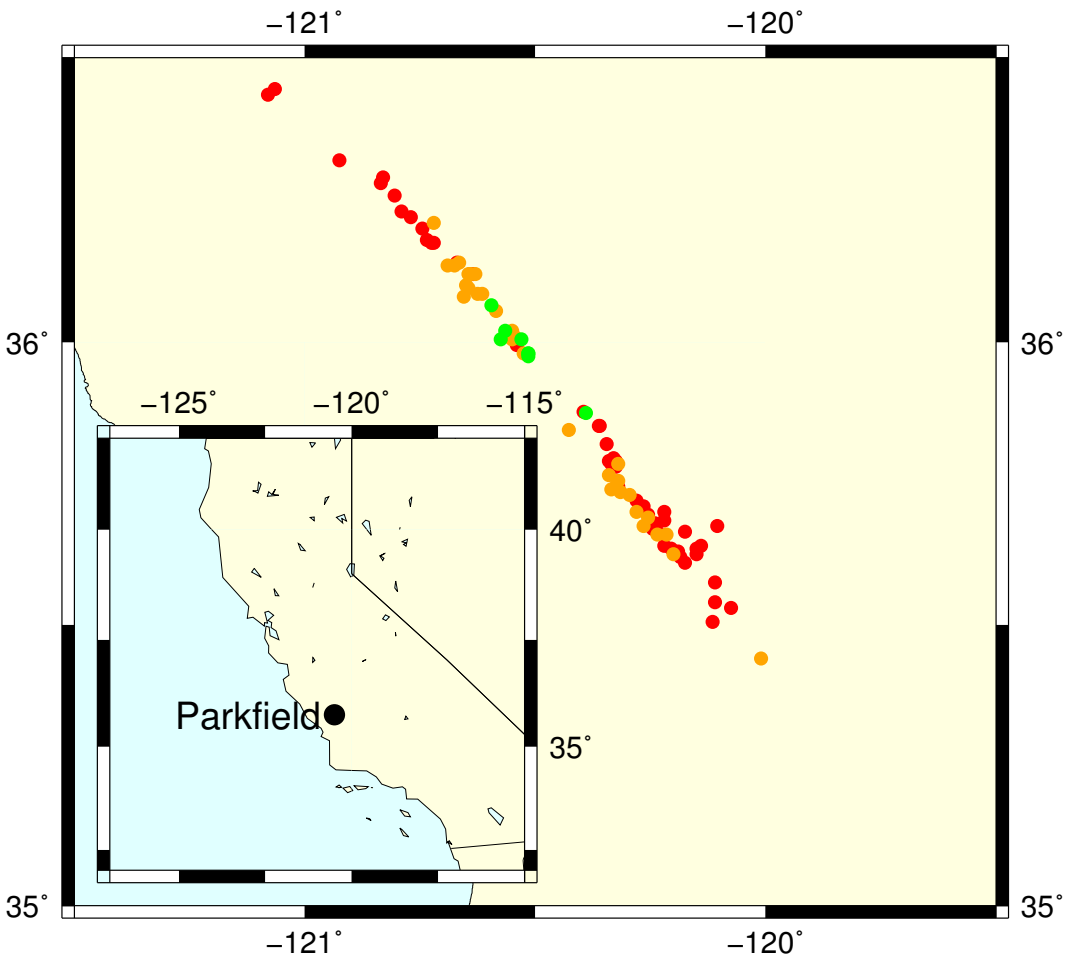

Figure 8: Fractional index for 88 low-frequency earthquakes families along the deep San Andreas fault (catalog by Shelly (2017 [60]). Red dots correspond to $0 < d < 0.1$. Orange dots correspond to $0.1 < d < 0.2$. Green dots correspond to $0.2 < d < 0.3$. Cyan dots correspond to $0.3 < d < 0.4$.

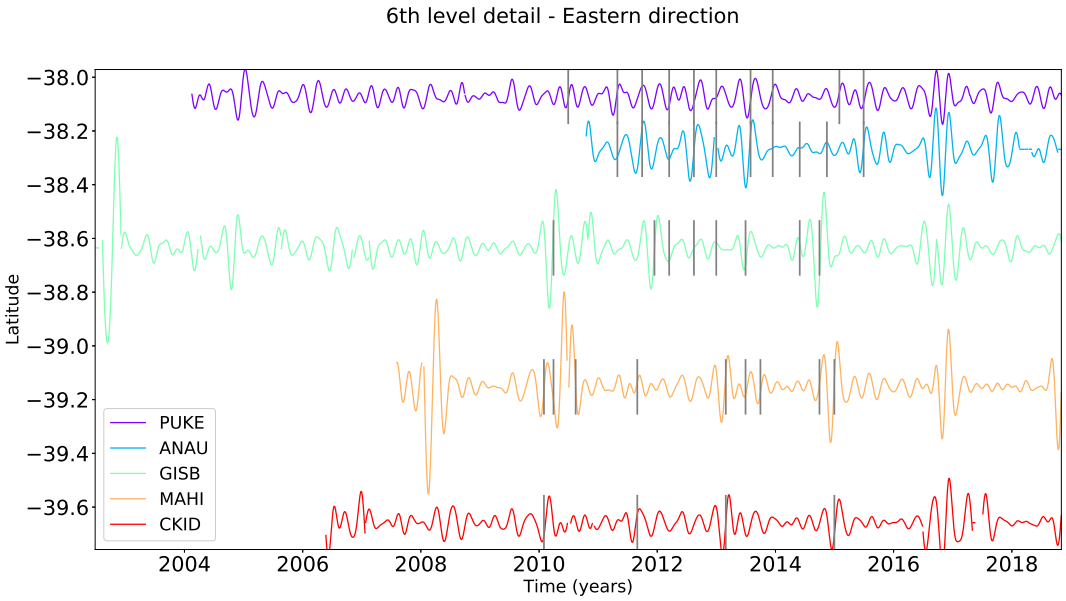

Figure 9: 6th level detail of the MRA for the eastern component of the time series recorded at stations PUKE, ANAU, GISB, MAHI, and CKID. The grey bars show the time of the transients listed by Todd and Schwartz (2016 [71], their Table 1).

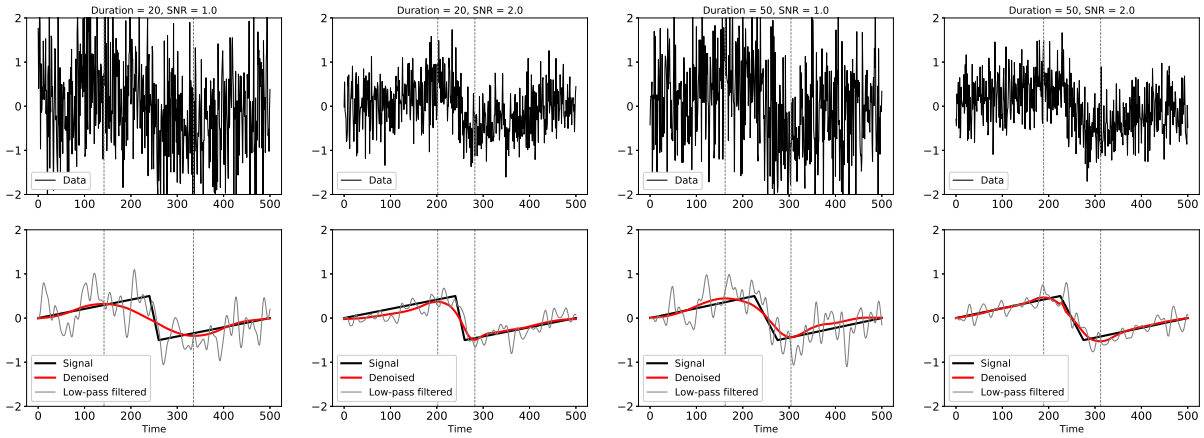

Figure 10: Denoising of synthetic time series using wavelets for two durations of the slow slip and two signal-to-noise ratios. The black line on the bottom panels is the signal. The black line on the top panels is the signal to which a Gaussian noise has been added. The red line on the bottom panels is the denoised signal obtained using thresholding of the wavelet vectors. The two vertical dashed lines show the time of the maxima and minima of the denoised signal. The grey line on the bottom panels is the signal obtained with a low-pass filter.

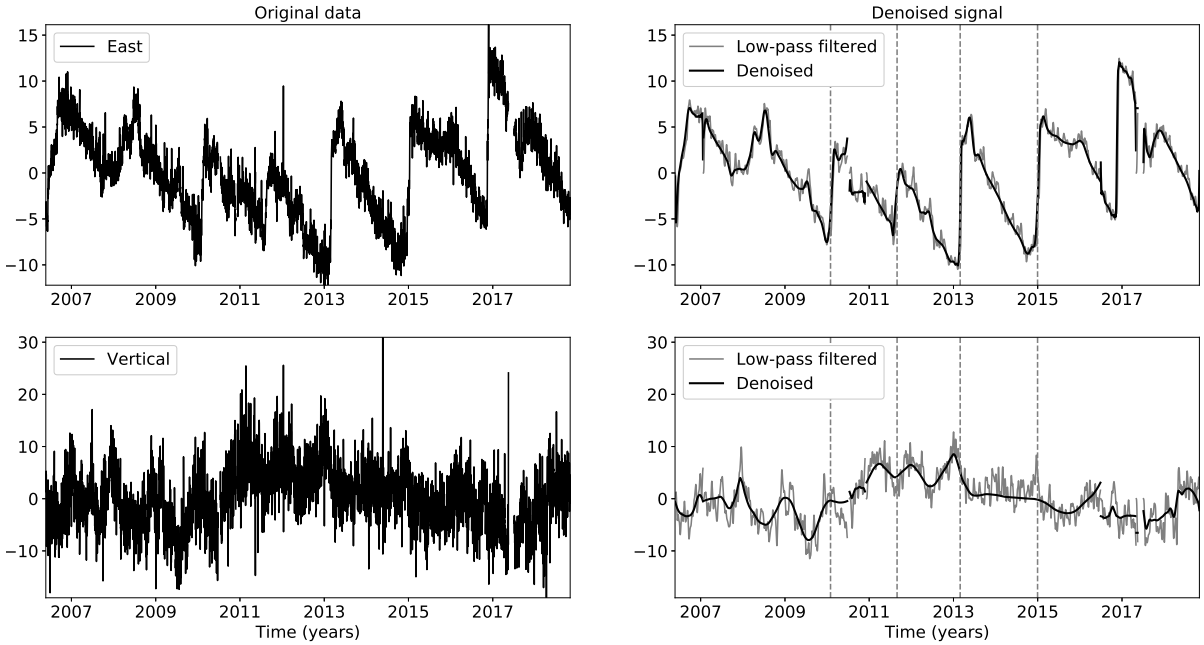

Figure 11: Original (left) and denoised (right) displacement observed at GPS station CKID for the eastern (top) and vertical (bottom) components. The black line on the right panels is the denoised signal obtained using thresholding of the wavelet vectors. The grey line on the right panels is the signal obtained with a low-pass filter. The vertical dashed lines indicate the timing of the slow slip events identified by Todd and Schwartz (2016 [71]).